J. Fluid Mech. (1989), *vol.* 199, *pp.* 89–124
Printed in Great Britain

Multiple-contour-dynamic simulation of eddy scales in the plane shear layer

By P. A. JACOBS AND D. I. PULLIN
Department of Mechanical Engineering, University of Queensland, St Lucia 4067, Australia

(Received 8 December 1987 and in revised form 23 June 1988)

The method of contour dynamics (CD) is applied to several inviscid prototype flows typical of the motions found in the transition region of the free shear layer. Examples of the interaction between the fundamental streamwise-layer perturbation and its first subharmonic are presented that illustrate the events of pairing and tearing of two rolled-up cores and also the coalescence of three rolled-up cores. The present simulations of the temporally unstable two-dimensional layer, at effectively infinite Reynolds number, support the hypothesis that the dynamics of the large-scale roll-up is only weakly dependent on Reynolds number. However, we find fine-scale structure that is not apparent in previous simulations at moderate Reynolds number. Spiral filaments of rotational fluid wrap around the rolled-up vortex cores producing 'spiky' vorticity distributions together with the entanglement of large quantities of irrotational fluid into the layer. Simulations proceeded only until the first such event because we were unable to resolve the fine detail generated subsequently. The inclusion of prescribed vortex stretching parallel to the vortex lines is found to accelerate the initial roll-up and to enhance the production of spiral vortex filaments. In the fundamental-subharmonic interaction, vortex stretching slows but does not prevent pairing.

1. Introduction

Numerical simulations of temporal two-dimensional mixing/shear layers have successfully provided structural models and examples of various flow features observed in experiments. These include the nonlinear roll-up of the nearly plane layer into compact vortex cores, the pairing of vortex structures and resulting growth in thickness of the layer. Aref (1983) reviews the application of vortex-element methods to the two-dimensional simulation of the mixing/shear layer.

A realistic model of the shear layer, based on solutions to the full Navier–Stokes equations, would have both a finite-thickness (δ) layer and a finite viscosity (ν) fluid. However, the range of Reynolds number (Re) obtainable in even two-dimensional numerical simulations is severely restricted owing to the computational burden of accurately resolving the fine-scale motions. Hence, most computational studies which aim to be relevant to high Re have either used a model in which both $\delta \to 0$ and $\nu \to 0$ (a vortex-sheet of zero thickness) or a model having $\delta > 0$ and $\nu \to 0$ (a finite-thickness inviscid vortex layer).

The approximation of the layer as a vortex sheet has been investigated by Damms & Kuchemann (1974) and Higdon & Pozrikidis (1985) among others. This model is apparently not well posed and there is now substantial evidence which suggests that the evolution of the vortex sheet results in the formation of a singularity in the sheet curvature in a finite critical time $t = t_c$ (Moore 1979; see also Meiron, Baker & Orszag

1982; Krasny 1986*a*). The sheet evolution beyond t_c remains an open question although the so-called 'δ-model' calculations of Krasny (1986*b*) give some support to the conjecture that a compact vortex spiral forms at $t = t_c^+$. If correct, this may save the vortex-sheet model in the mathematical sense but would leave the numerical analyst with the formidable problem of accurately calculating the vortex spiral structure in the simulations for $t > t_c^+$. Note that Moore (1978) has considered a layer of small but finite δ but the relevant equation of motion admits spurious short-wave instabilities.

The second approach of keeping δ finite and setting $\nu = 0$ appears to be a well-defined limit (for a uniform vortex layer this is also an open question owing to possible fine-scale filamentation of the vorticity interface; see e.g. Dritschel 1987) and may also be a more realistic physical representation of the early stages of an experimental shear layer at very large Re. In studying solutions to this model, we suppose that for finite times in strictly two-dimensional flow, the limiting solution to the Navier–Stokes equations (in the absence of solid boundaries) as $Re \to \infty$ (or as $\nu \to 0$) is equivalent to the solution of the incompressible Euler equations starting with the same initial conditions (vorticity field) (see e.g. Saffman & Baker 1979). Hence, we assume that the inviscid simulations in the following discussion will be relevant to the behaviour of the layer as $Re \to \infty$.

The definition of the vorticity field and the appropriate Reynolds number in solutions of the plane Navier–Stokes equations are closely linked with the numerical technique. The simulations of finite-thickness layers have usually been based on flow models having either (i) continuous vorticity distribution at low to moderate Re (finite-difference or spectral methods), (ii) discrete vorticity distributions such as a cloud of point vortices or vortex blobs, or (iii) a step-function distribution such as used in the contour-dynamics (CD) method (Zabusky, Hughes & Roberts 1979) at effectively $Re \to \infty$.

Short-time simulations showing the fine details of one amalgamation event have been performed by Patnaik, Sherman & Corcos (1976), Acton (1976) and Riley & Metcalfe (1980). These studies have mainly concentrated on the interaction of the fundamental perturbation combined with its first subharmonic which may be expected to have maximum growth rate (Pierrehumbert & Widnall 1982). Although the simulations of both Riley & Metcalfe (spectral method) and Patnaik *et al.* (using the finite-difference method) were limited to $Re_\delta = O(100)$, they still produced vortex-pairing scenarios similar to those produced in the point-vortex simulation of Acton. The vortex tearing mechanism (Moore & Saffman 1975) was also examined in these simulations and was found to occur over a longer timescale and be weaker than the pairing interaction in cases where both effects were present.

Several 'long-time' numerical simulations have been performed which provide vortex histories over timescales spanning several vortex lifetimes. Ashurst (1977) used a vortex-blob technique in which vortex elements were ejected into the flow at the trailing edge of a splitter plate and were allowed to evolve as they convected downstream. Ashurst showed that the dominant mechanism for the production of the larger structures was by pairing of the smaller cores (or clouds of vortex elements). Aref & Siggia (1980) performed a simulation of the spatially periodic shear layer using the cloud-in-cell (CIC) technique with 4096 vortex elements. They provided statistical estimates of the layer properties and suggested that the growth of the cross-stream thickness was due, in part, to the scattering of the vortex cores about the centreline of the layer. The initial conditions at the splitter plate were

disturbed with combinations of the primary eigenfunction and its subharmonics and vortex histories showed examples of pairing and tearing of the vortex cores.

In this paper we shall use the inviscid CD formulation for an x-periodic vorticity layer to produce moderate time, high-resolution simulations of the temporal shear-layer evolution at $Re_\delta = \infty$ without the inherent 'graininess' of the vortex-element techniques. The first such simulation of this type known to us is that by Pozrikidis & Higdon (1985) who used a model consisting of a single finite-thickness layer of uniform vorticity. Presently, we shall investigate the evolution of a non-uniform-vorticity layer, defined by a piecewise-constant vorticity distribution, which is initially disturbed by imposing one or more eigenfunction modes, as calculated by a linear analysis, with small but finite amplitudes. Such nearly continuous distributions are representative of the ensemble-averaged vorticity fields measured by Browand & Weidman (1976) and Oster & Wygnanski (1982).

We base our prototype flows on the Corcos–Lin–Sherman (CLS) model in which the temporal shear layer is defined as a short hierarchy of deterministic motions interacting via a system of identifiable nonlinear instabilities (Corcos & Sherman 1984; Corcos & Lin 1984; Lin & Corcos 1984). Each level of motion in the hierarchy is characterized by a specific vorticity distribution evolving within the ambient strain environment provided by the other scales of motion. The first tier (or first-order motion) is the standard temporal two-dimensional instability and characteristic roll-up of the layer into vortex structures whose axes are aligned in the spanwise direction (the primary vortices). The secondary vortices are modelled as an array of highly flattened, counter-rotating vortices (with axes aligned in the streamwise direction) evolving in the local strain environment provided by the primary vortices. A CD simulation of this vorticity distribution has been attempted by Pullin & Jacobs (1986). The third tier of deterministic motions is composed of the small-scale eddies that evolve on the secondary streamwise vortices. For increasing Re, the secondary vortices will become very thin and, on a small scale, the local environment will be similar to that of an infinite vortex layer embedded in a stretching strain field. Such a stretched layer may be expected to be unstable to spanwise perturbations and lead to the production of tertiary motions (Lin & Corcos 1984). Hence, we expect that the evolution of a stretched shear layer will be relevant to the tertiary motions when the aspect ratio of the secondary vortices becomes large. At low Re these motions may not evolve as the viscous diffusion/stretching strain balance of the Burgers-like vorticity distribution is achieved in a short time but, for $Re \to \infty$, we conjecture that several tiers of higher-order structures will rapidly generate motions needed for the energy cascade to smaller scales characteristic of inertial-range turbulence.

2. Formulation

2.1. *Flow configuration*

We shall study numerically the nonlinear evolution of initial vorticity distributions of the type illustrated in figure 1. These will model the initial (perturbed) state of the temporal shear layer. The two-dimensional vortex layer is periodic in the x-direction, y is the cross-stream direction and z is the spanwise direction (of the shear layer). Only one streamwise wavelength $0 \leqslant x \leqslant \lambda_c$ of the x-periodic computational domain is shown and this contains circulation Γ_c. The initial vorticity

$$\boldsymbol{\omega} = \omega(y)\,\boldsymbol{k}, \tag{1}$$

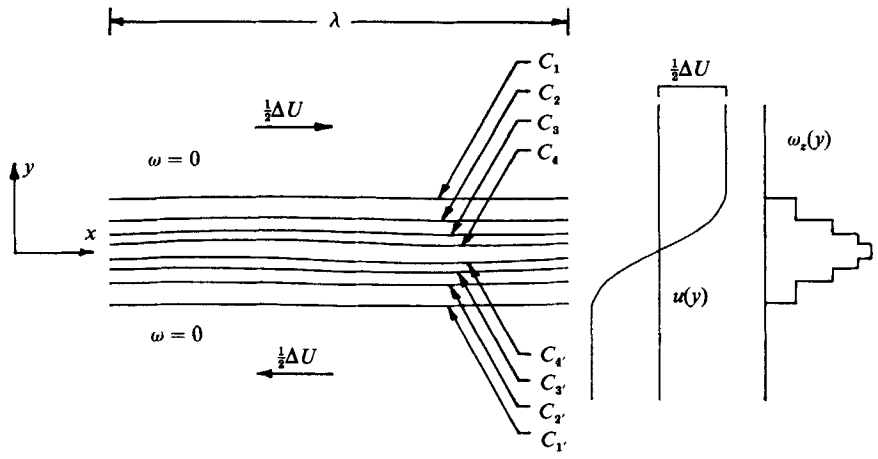

FIGURE 1. A single wavelength of an x-periodic shear layer consisting of $M = 4$ uniform-vorticity regions. The bounding contours (primed subscripts indicate contours below the x-axis) are disturbed by a small-amplitude perturbation. The associated mean x-velocity field, $u(y)$ and vorticity cross-section are shown to the right.

of the undisturbed layer is a piecewise-constant distribution with regions, R_j, $j = 1 \ldots M, 1' \ldots M'$ containing fluid with vorticity ω_j in both regions R_j and $R_{j'}$. The primed indices here indicate contours that are positioned at y-stations initially below the x-axis. Each contour above the x-axis has a corresponding contour below the axis. The associated velocity field, $u_x(y)$, varies piecewise-linearly from $+\Delta U/2$, $y > h_1/2$ to $-\Delta U/2$ for $y < -h_1/2$, where h_j is the average distance between the contours, C_j, $j = 1 \ldots M$, $1' \ldots M'$ (which delineate the discontinuities of the double-staircase vorticity profile). The contours are labelled C_1 to C_M progressing from the top to the middle of the layer (and $C_{1'}$ to $C_{M'}$ for the lower contours). Hence, the regions R_j, $j = 1 \ldots M-1$ are bounded by contours C_j and C_{j+1} with R_M (being the same region as $R_{M'}$) bounded by C_M and $C_{M'}$. Specific ω-distributions across the layer will be discussed in §4.

2.2. *Contour dynamics*

We utilize the contour-dynamic (CD) technique (Zabusky *et al.* 1979), which is suitable for the simulation of 'almost-continuous' vorticity fields in a two-dimensional flow of an inviscid fluid. We consider an initial vorticity field with only one component of vorticity

$$\boldsymbol{\omega} = \omega(x, y, t = 0)\,\boldsymbol{k}, \tag{2}$$

and its associated two-dimensional velocity field

$$\boldsymbol{u} = V_x \boldsymbol{i} + V_y \boldsymbol{j}, \tag{3}$$

where $(\boldsymbol{i}, \boldsymbol{j}, \boldsymbol{k})$ are the unit vectors along the Cartesian axes. Using $\nabla \cdot \boldsymbol{u} = 0$ for an incompressible fluid and $\boldsymbol{\omega} = \nabla \times \boldsymbol{u}$ it follows that, V_x and V_y may be derived kinematically from a cylindrically symmetric vorticity field.

The vorticity field is embedded in an irrotational uniform strain field

$$\boldsymbol{u}_s = -\gamma(t)\, y\boldsymbol{j} + \gamma(t)\, z\boldsymbol{k}, \tag{4}$$

where $\gamma(t)$ is an arbitrary strain rate which we shall assume is a specified function of time. Positive $\gamma(t)$ will stretch the vorticity in the z-direction. The full velocity field

is $\boldsymbol{u}+\boldsymbol{u}_s$ and, when substituted into the vorticity transport equation with $\nu = 0$, gives

$$\frac{\mathrm{D}\omega}{\mathrm{D}t} = \gamma(t)\,\omega. \tag{5}$$

The solution to (5) along particle paths $x(t)$, $y(t)$ is

$$\omega[x(t), y(t), t] = \omega[x(0), y(0), 0]\exp[Q(t)], \tag{6a}$$

$$Q(t) = \int_0^t \gamma(t')\,\mathrm{d}t', \tag{6b}$$

where $\omega[x(0), y(0), 0]$ is the initial vorticity. Equations (6a, b) represent the intensification of particle vorticity (for $\gamma(t) > 0$) by the z-component of the applied strain field. We now choose the vorticity field to be the piecewise-constant distribution of §2.1 and let $\zeta_j(e) = x_j(e)+\mathrm{i}y_j(e)$ denote a material point on C_j. Identifying the velocity $\mathrm{d}\zeta_j^*/\mathrm{d}t$ (* ≡ conjugate) with the Eulerian velocity field, we obtain the CD equation for the evolution of C_j as (Pullin & Jacobs 1986)

$$\frac{\partial\zeta_j^*}{\partial t} = \mathrm{i}\gamma(t)\,y_j + \frac{\exp[Q(t)]}{2\lambda_c i}\sum_{m=1}^{M}\Delta\omega_m(0)\int_{\mathscr{C}_m}(y_j - y_m')\cot\left[\frac{\pi}{\lambda_c}(\zeta_j-\zeta_m')\right]\mathrm{d}\zeta_m', \quad j = 1\ldots M, \tag{7}$$

where $\Delta\omega_m(0) = \omega_m(0)-\omega_{m-1}(0)$. The summation is over all nested contours $\mathscr{C}_m = C_m + C_{m'}$, $m = 1\ldots M$.

For the simulation of the nominally two-dimensional flow of the temporal shear layer, we may set the stretching $\gamma = 0$ and recover the purely two-dimensional CD equations. Stretching does not allow the creation of vorticity. Hence, the circulation Ω_j of region R_j is an invariant of the flow and, from (6), the area A_j enclosed by C_j and C_{j+1} varies as

$$A_j(t) = A_j(0)\exp[-Q(t)]. \tag{8}$$

3. Numerical implementation

There are four major sections to the implementation of the CD equations:

(i) Each continuous contour is discretized by defining it as a set of nodes connected by line segments. This produces a finite set of ordinary differential equations (ODEs) suitable for a numerical implementation.

(ii) The line integral in (7) is evaluated either analytically or by numerical quadrature over each small segment and then summed.

(iii) The solution is stepped forward in time using a standard technique for first-order ODEs.

(iv) The node set is (occasionally) updated to ensure that the segmented contour description remains adequate.

We first discretize the C_j, $j = 1\ldots M$, by defining each contour by a set of N_j nodes $(\zeta_j)_k$, $k = 0\ldots N_j(t)$, $j = 1\ldots M$, with $(\zeta_j)_0 = (\zeta_j)_N \pm \lambda_c$ (i.e. open contours) for the contours C_j and $C_{j'}$, respectively, of the vortex layer. Joining subsets of two or three of these nodes are $NSEG_j$ segments describing C_j with a local interpolating polynomial. The velocities of the $(\zeta_j)_k$ are then evaluated by summing the contributions of each interpolated segment, thus giving a set of $2N$,

$$N = \sum_{j=1}^{M} N_j(t), \tag{9}$$

ODEs for the node coordinates, $((x_j)_k, (y_j)_k)$. These segments of the C_j are defined locally by interpolating curves on node subsets with parameter e. For the simulations reported here, we choose the interpolating segments to be parabolic curves

$$\zeta(e) = Ae^2 + Be + C, \quad -1 \leqslant e \leqslant 1$$

defined on subsets of three adjacent nodes with

$$\zeta(e=-1) = (\zeta_m)_{n-1}, \quad \zeta(e=0) = (\zeta_m)_n, \quad \zeta(e=1) = (\zeta_m)_{n+1}.$$

Other interpolation methods include circular arcs fitted to node subsets (Pozrikidis & Higdon 1985) and cubic splines (Dritschel 1988). Adequate resolution is required for conservation of the flow invariants such as the total circulation and also for maintaining contour flexibility. We found that the C_j were inflexible if the segment sizes were significantly larger than the lengthscales associated with the velocity variations. Dritschel (1988) suggests that there is also an advantage in having a description (e.g. cubic spline) that does not introduce discontinuities in the contour curvature. We note that parabolic segments do so.

The equations of motion for the node coordinates contain integrals over the interpolating segments which cannot be obtained in closed form. Also, the integrand behaves in a weakly singular manner over segments that approach the velocity point $(\zeta_j)_k$, closely. Dritschel (figure 13, 1986) illustrated the numerical instability that is related to the inaccurate evaluation of the velocities via a numerical quadrature. Increasing the order of the quadrature delayed the appearance of the instability but did not eliminate it. To avoid these difficulties in 'close approach' integrations, we introduce an 'analytic patch' procedure in which we decompose the integrand into a simple part that varies rapidly but can be integrated analytically, and a slowly varying (but more complex) part that can be accurately integrated with a 4-point Gauss–Legendre quadrature. Further details are included in the Appendix. Where the close-approach approximation is not required, we use the fixed-rule quadrature only. The ODE solver utilized was a packaged 4, 5th–order Runge–Kutta–Fehlberg routine (RKF45) from the text Forsythe, Malcolm & Moler (1977). The single-step truncation error tolerance, ϵ_{de}, was specified on entry to the routine and for most calculations was set to 10^{-4}.

The node update scheme is essentially that described in Jacobs & Pullin (1985) and Pullin & Jacobs (1986). Briefly, a node was inserted between $(\zeta_j)_k$ and $(\zeta_j)_{k+1}$ on C_j if

$$|(\zeta_j)_{k+1} - (\zeta_j)_k| > \epsilon_{\mathrm{ni}}, \tag{10}$$

where ϵ_{ni} is determined by a set of criteria based on the local curvature and proximity of other contour sections. The new node was placed at $e = k+0.5$ by linear interpolation on $[(\zeta_j)_k, (\zeta_j)_{k+1}]$. The node deletion scheme operated by deleting node $(\zeta_j)_k$ if

$$|(\zeta_j)_{k+1} - (\zeta_j)_k| < \epsilon_{\mathrm{nd}} \tag{11}$$

where ϵ_{nd} is a specified fraction of ϵ_{ni} or an absolute lower limit. This simple node-deletion procedure was preferred to one involving higher-order interpolation as we found by experience that it tended to reduce the occurrence of slender filaments containing negligible circulation and decreased the tendency for contours to fold back upon themselves.

	j	$\hat{\omega}_j$	$\frac{1}{2}\hat{h}_j$
(*a*)	1	−0.0502	0.7290
	2	−0.1179	0.4375
	3	−0.1592	0.2550
	4	−0.1819	0.1180
(*b*)	1	−0.0130	0.8230
	2	−0.0300	0.7078
	3	−0.0529	0.6008
	4	−0.0811	0.5020
	5	−0.1092	0.4033
	6	−0.1370	0.3127
	7	−0.1671	0.2140
	8	−0.1857	0.1152

TABLE 1. Dimensionless piecewise-constant vorticity profile for the upper half of the unperturbed shear layer. Lengthscale = $\lambda_c/(2\pi)$, timescale = $\lambda_c^2/(4\pi^2\Gamma_c)$, $\lambda_c = \lambda_1$; (*a*) $M = 4$, $k_1\delta_\omega = 0.875$; (*b*) $M = 8$, $k_1\delta_\omega = 0.857$.

Qualitative checks upon the solution accuracy were made by monitoring the fractional error in the circulation invariants for each uniform-vorticity region

$$\Delta(\Omega_j) \equiv \frac{\exp(Q(t))\,A_j(t) - A_j(0)}{A_j(0)}. \tag{12}$$

Unfortunately, $\Delta(\Omega_j)$ is fairly insensitive to the fine-scale coherence of the C_j, while higher-order vorticity invariants such as those associated with linear and angular momentum conservation and energy conservation are difficult to calculate to the required accuracy. We found that the most reliable way of testing the accuracy of the method is to demonstrate convergence of the solution contours with respect to the node-adjustment parameters (which determine $N_j(t)$). Examples of convergence for the stretched shear layer were performed and are discussed subsequently.

4. Initial conditions

4.1. *Initial vorticity distribution*

The undisturbed, or basic, piecewise-constant $\omega(y)$-distribution was chosen to approximate the Gaussian curve

$$\omega(y) = A\exp[-\rho(y/h_1)^2], \tag{13}$$

where ρ and A are constants. We denote dimensionless forms of h and ω by $\hat{h}$ and $\hat{\omega}$ respectively, based on the lengthscale $L = \lambda_c/2\pi$ and timescale $T = \lambda_c^2/(4\pi^2\Gamma_c)$. Numerical values of $\hat{\omega}$ and $\hat{h}$ for our present approximation to (13) in $y > 0$ with $M = 4$ and $M = 8$ are given in tables 1(*a*) and 1(*b*) respectively. We define the vorticity thickness $\delta_\omega = \Delta U/\omega_{\max}$, where $\omega_{\max} = \partial U/\partial y|_{\max}$ occurs at the midpoint of the layer. The means of scaling the $\omega(y)$-distribution in the y-direction by choice of δ_ω will be discussed subsequently.

4.2. *Initial disturbance: linearized analysis*

Initial conditions for the CD simulations were provided by superimposing vorticity-preserving disturbances on the basic flow. These took the form of x-periodic contour perturbations given by

$$\boldsymbol{\eta}(x,t) = \tfrac{1}{2}\boldsymbol{h} + \sum_{n=1}^{N} a_n \boldsymbol{f}_n^{(M)} \exp(\mathrm{i}\sigma\tau) \exp(\mathrm{i}k_1[x/n + \phi_n]) \tag{14a}$$

where a_n and ϕ_n are arbitrary scaling amplitudes and phase shifts respectively, and

$$\boldsymbol{\eta} = [\eta_1 \ldots \eta_M, \eta_{M'} \ldots \eta_{1'}]^{\mathrm{T}}, \tag{14b}$$

$$\boldsymbol{h} = [h_1 \ldots h_M, h_{M'} \ldots h_{1'}]^{\mathrm{T}} \tag{14c}$$

$$\boldsymbol{f}^{(M)} = [\alpha_1 \ldots \alpha_M, \alpha_{M'} \ldots \alpha_{1'}]^{\mathrm{T}}. \tag{14d}$$

In (14a) $\eta_j(x,t)$ is the y-coordinate for C_j, $\alpha_j = \alpha_{\mathrm{r}j} + \mathrm{i}\alpha_{\mathrm{i}j}$ is the complex amplitude, $k_1 = 2\pi/\lambda_1$ is the wavenumber of the fundamental disturbance and $\sigma = \sigma_{\mathrm{r}} + \mathrm{i}\sigma_{\mathrm{i}}$ is the complex growth rate ($-\sigma_{\mathrm{i}}$ = growth rate, σ_{r}/k = phase speed) of the perturbation. T is the transpose. Equation (14a) is a sum consisting of a fundamental of wavelength λ_1 plus $N-1$ subharmonics. Hence $\lambda_{\mathrm{c}} = N\lambda_1$. The fundamental is determined by solving the x-periodic temporal stability problem for the unperturbed flow, which is equivalent to solving the Rayleigh stability equation for the undisturbed piecewise-constant ω-distribution. This was done by substituting (14a) with $N = 1$, $\phi_1 = 0$, and equivalent expressions for the perturbed velocity fields into the Euler equations and linearizing in a_{i} thus giving an eigenvalue problem with eigenvalue σ and α_j, $j = 1 \ldots M$, $1' \ldots M'$ as part of the associated eigenfunction. Details of this linear stability analysis of the piecewise-constant vorticity profiles are contained in Jacobs (1987).

Figure 2 shows the normalized growth rate ($-\sigma_{\mathrm{i}}/\omega_{\max}$) for the four vorticity profiles: (*a*) the uniform-vorticity layer $M = 1$ previously studied by Rayleigh (1880) and more recently by Pozrikidis & Higdon (1985); (*b*) the piecewise-constant $M = 4$ vorticity profile (table 1*a*); (*c*) the piecewise-constant $M = 8$ vorticity profile (table 1*b*); and (*d*) the continuous vorticity profile corresponding to the tanh velocity profile studies by Michalke (1964). For all profiles, there are unstable perturbations only for a limited range of $k\delta_\omega$. All solutions that have $\sigma_{\mathrm{i}} \neq 0$ also have $\sigma_{\mathrm{r}} = 0$ indicating that unstable distrubances do not progress along the layer.

We normalize the numerical values for the α_j such that the contour with largest displacement has magnitude $|\alpha| = 1.0$. (The contour of maximum amplitude is always the innermost contour C_M, $C_{M'}$.) The normalization procedure also imposes a symmetry $\alpha_{j'} = -\alpha_j^*$ where * represents the complex conjugate. It follows that the initial contour perturbations, and hence the subsequent contour evolution determined by (7), are invariant under (x,y)-axis rotations of $n\pi$ radians.

Corcos & Sherman (1984) report that an early consequence of nonlinearity in the vortex dynamics is the selection of a dominant wavelength. There is experimental evidence (e.g. Thorpe 1971) to suggest that, early in the evolution, a single wavelength dominates the growth and temporarily inhibits the growth of perturbations having similar wavelengths but with either smaller growth rates (σ_{i}) or smaller initial amplitudes (α_0). It thus seems reasonable to use initial conditions that are simpler than a perturbation with a continuous wavenumber spectrum and have only, say, two or three linearly combined eigenfunctions ($N = 2$ or $N = 3$ in

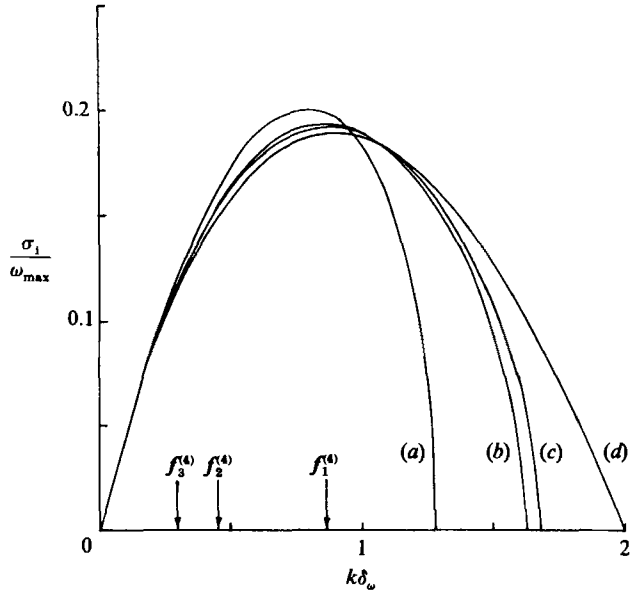

FIGURE 2. Normalized growth rates for four vorticity distributions: (*a*) single region, $M = 1$, of uniform vorticity; (*b*) $M = 8$ piecewise-constant vorticity profile; (*c*) $M = 4$ piecewise-constant vorticity profile; (*d*) hyperbolic-tangent velocity profile (Michalke 1964). The primary mode, first subharmonic, and second subharmonic for the $M = 4$ vorticity profile are labelled $f_1^{(4)}$ $f_2^{(4)}$ and $f_3^{(4)}$ respectively.

		α_j		
(*a*)	j	$f_1^{(4)}, (k\delta_\omega = 0.875)$	$f_2^{(4)}, (k\delta_\omega = 0.438)$	$f_3^{(4)}, (k\delta_\omega = 0.292)$
	1	−0.248–i0.339	−0.194–i0.652	−0.143–i0.762
	2	−0.331–i0.479	−0.211–i0.772	−0.151–i0.842
	3	−0.393–i0.667	−0.206–i0.883	−0.137–i0.931
	4	−0.341–i0.940	−0.137–i0.991	−0.0843–i0.997

		α_j	
(*b*)	j	$f_1^{(8)}, (k\delta_\omega = 0.867)$	$f_2^{(8)}, (k\delta_\omega = 0.429)$
	1	−0.220–i0.315	−0.176–i0.621
	2	−0.248–i0.355	−0.188–i0.660
	3	−0.276–i0.397	−0.194–i0.701
	4	−0.306–i0.448	−0.206–i0.738
	5	−0.339–i0.511	−0.210–i0.786
	6	−0.370–i0.595	−0.209–i0.841
	7	−0.386–i0.735	−0.215–i0.887
	8	−0.329–i0.994	−0.131–i0.991

TABLE 2. Complex amplitudes for fundamental $f_1^{(4)}$, first subharmonic $f_2^{(4)}$ and second subharmonic $f_3^{(4)}$ eigenmodes from linear analysis. (*a*) $M = 4$, (*b*) $M = 8$.

(14)). The fundamental mode is chosen to be the perturbation with maximum rate of growth in figure 2 and is labelled as $f_1^{(M)}$. For $M = 4$, $k_1 \delta_\omega = 0.875$, while for $M = 8$, $k_1 \delta_\omega = 0.857$. We note that fixing $k_1 \delta_\omega$ fixes the y-scale of the ω-distribution for the fundamental mode given in table (1*a*, *b*). In figure 2 the fundamental, first subharmonic, and second subharmonic modes for the $M = 4$ profile are indicated by

Case	$N = \frac{\lambda_c}{\lambda_1}$	M	Perturbation	Comment
1	1	1	$0.05f_1^{(1)}$	Uniform vorticity layer
2	1	4	$0.05f_1^{(4)}$	Non-uniform vorticity layer
3	2	4	$0.10f_1^{(4)}+0.10f_2^{(14)}$	Pairing interaction
3*a*	2	4	as for 3	Single precision
4	2	8	$0.10f_1^{(8)}+0.10f_2^{(8)}$	Pairing interaction
5	2	4	$0.10f_1^{(4)}+0.10\,e^{i\pi/2}f_2^{(4)}$	Tearing interaction
6	2	4	$0.10f_1^{(4)}+0.10\,e^{i\pi/4}f_2^{(4)}$	Combined pairing/tearing
7	3	4	$0.10f_1^{(4)}+0.10f_3^{(4)}$	Three-vortex coalescence

TABLE 3. Summary of two-dimensional shear-layer simulations ($\hat{\gamma}_3 = 0$). Perturbation amplitudes are scaled as $\alpha_n k_1$. All computations used 14-figure arithmetic except for 3*a*. λ_c = length of computational domain; λ_1 = fundamental wavelength.

$f_1^{(4)}, f_2^{(4)}$, and $f_3^{(4)}$ respectively. Table 2(*a*) contains the numeric vales for the α_j in the upper half of the layer (i.e. α_j, $j = 1 \ldots 4$) for the $M = 4$ profile, while table 2(*b*) contains the data defining the fundamental and first subharmonic eigenfunctions for the $M = 8$ profile.

4.3. *Choice of a_n and f_n*

All present computations were performed with $N = 1$, 2 or 3. Table 3 gives a summary of the various mode combinations according to (14*a*) that were used in the present simulations, and also shows values of the a_n and ϕ_n used in the various cases. Consider the superposition of only the fundamental $f_1^{(M)}$ plus the first subharmonic $f_2^{(M)}$ ($N = 2$). Choosing $\phi_1 = 0$, the effect of $f_2^{(M)}$ depends on ϕ_2, and owing to x-periodicity in $0 < x \leqslant \lambda_c = 2\lambda_1$, we need only consider the range $0 \leqslant \phi_2 \leqslant \frac{1}{2}\pi$. We choose $\phi_2 = 0, \frac{1}{4}\pi, \frac{1}{2}\pi$, which can be shown to correspond to the well-known pure pairing mode, pairing/tearing mode and the pure tearing modes respectively. Referring to the first frame of figure 3 with $N = 2$, $\phi_2 = 0$, $f_1^{(4)}$ redistributes the unperturbed vorticity to produce two slight accumulations which will later become the primary vortex cores with spacing λ_1. $f_2^{(4)}$ modulates the y-positions of the vortex-accumulation centroids while maintaining equal strength. With $\phi_2 = \frac{1}{2}\pi$ (figure 4), $f_2^{(4)}$ modulates the strengths of the vortex accumulations while maintaining their centroids undisturbed and, when $\phi_2 = \frac{1}{4}\pi$, $f_2^{(4)}$ alters both the accumulation strengths and the centroid positions.

Ideally we would like to choose the a_n sufficiently small so that the early layer evolution remains within the linear regime. The results of several numerical experiments indicated that the choice $a_n k_1 = 0.1$ was adequate in this respect and was used in all simulations with $N > 1$. Where $N = 1$ we used $a_1 k_1 = 0.05$.

5. Results and discussion

Most of the present simulations were done in 64-bit arithmetic on a Cyber 205 computer, while some were performed in 32-bit precision on an IBM 3083 computer. Sensitivity of the solutions to initial vorticity profile variations was checked by comparing particular $M = 4$ simulations with a uniform-vorticity ($M = 1$) layer (case 1, table 3) and an $M = 8$ layer (case 4). A separate computation, case 3*a* performed with an independent code (see Jacobs 1987) indicated that the simulations were broadly insensitive to the numerical implementation of the CD algorithm.

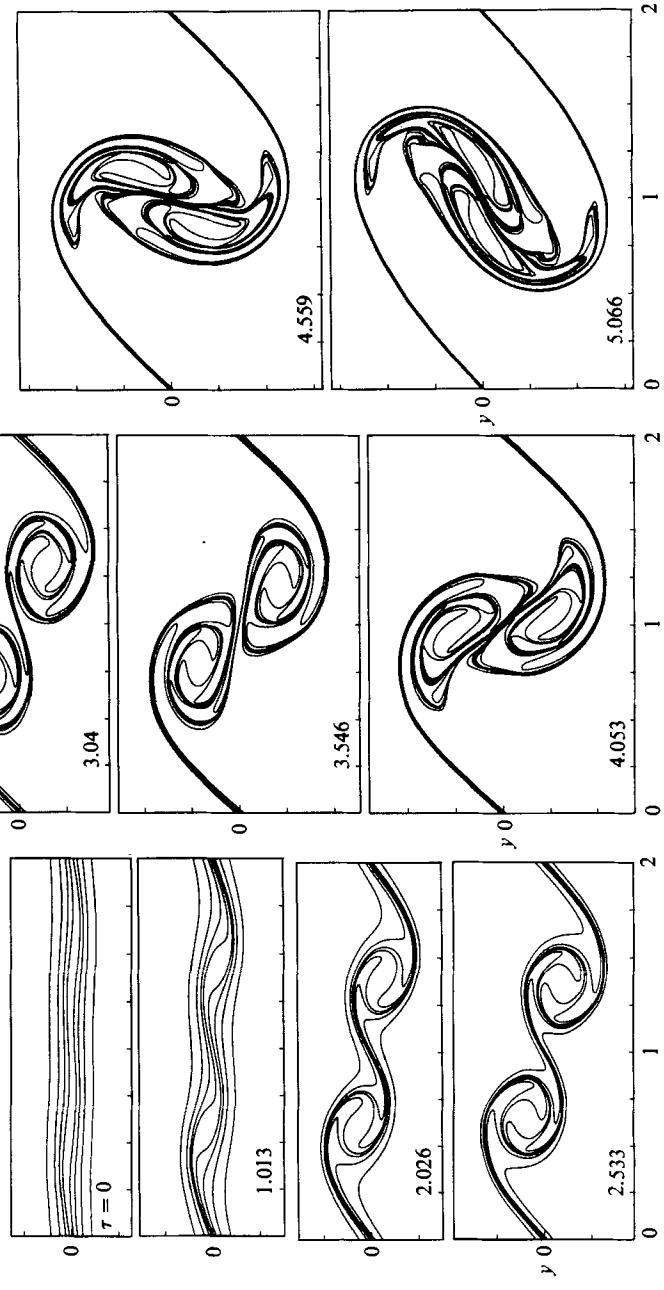

FIGURE 3. Evolution of the $M = 4$ shear layer showing a single pairing event. Initial perturbation $f_1^{(4)}+f_2^{(4)}$ (case 3, table 3). Times τ as shown.

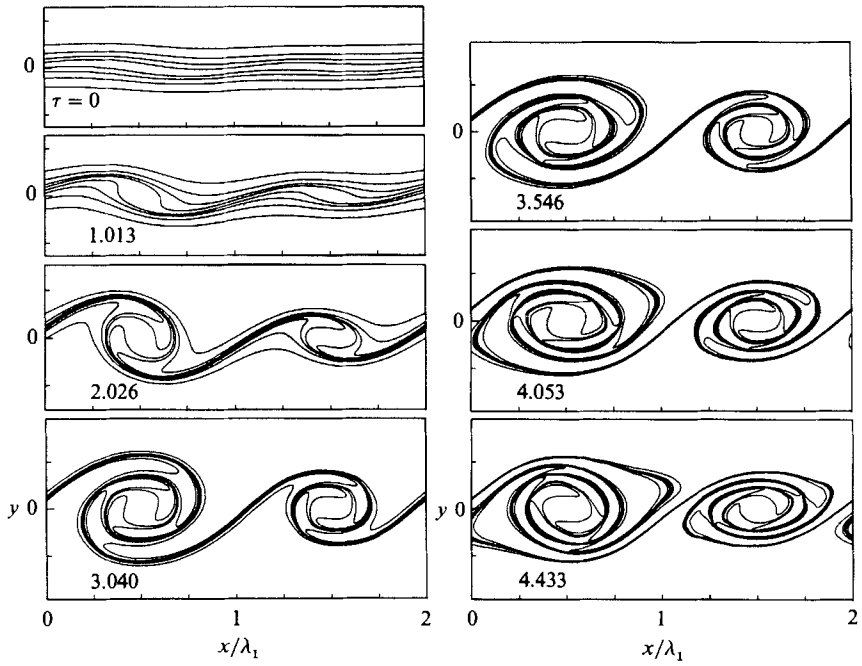

FIGURE 4. Evolution of $M = 4$ shear layer showing a tearing event. Initial perturbation $f_1^{(4)} + e^{i\pi/2} f_2^{(4)}$ (case 5, table 3). Times τ as shown.

Where possible (and convenient) we made use of the shear-layer symmetries and set the lower contours ($C_{j'}$) to be images of the upper contours, thus halving the computational effort required for the full nonlinear calculation. However, this could only be done for cases where the phase shift of all of the subharmonics was set to zero (cases 1, 2, 3, 3a, 4, 7 of table 3). Although case 5 has a similar form of symmetry, it was not implemented in the numerical code. Numbers of nodes on each contour ranged from $N_j(t = 0) = 60$, $j = 1 \ldots 4$ to typically $N_j(\tau_{\max}) = 527$, 718, 867, 957. (These figures are obtained from case 3.) The largest number of nodes always occurred on the innermost contours, which were invariably the longest. The maximum number of nodes allowed on the Cyber 205 runs was restricted to $N_{\max} = 1000$ and the IBM 3083 was restricted to $N_{\max} = 600$.

Each simulation takes place in a box of length $\lambda_c = N\lambda_1$ which contains circulation $\Gamma_c = N\Gamma_1$, where Γ_1 is the circulation associated with the fundamental. The actual computations were based on length- and timescales defined in §4.1 but it is convenient to discuss results in terms of a length-scale λ_1 and a dimensionless time $\tau = t/T_1$, where $T_1 = \lambda_1^2/\Gamma_1$. These scales are associated with the fundamental. Evolutionary histories are presented as sequences of snapshots of the bounding contours with increasing τ. The contours have been reconstructed from the node sets by joining consecutive nodes by straight-line segments. Although parabolic segments have been used in the calculations, the straight segments give a better idea of the segment size and contour resolution obtained.

Other information computed includes:

(i) normalized length of contour p_j giving a measure of the interfacial area of the two-dimensional layer and hence mixing;

(ii) maximum height of contours Y_j;

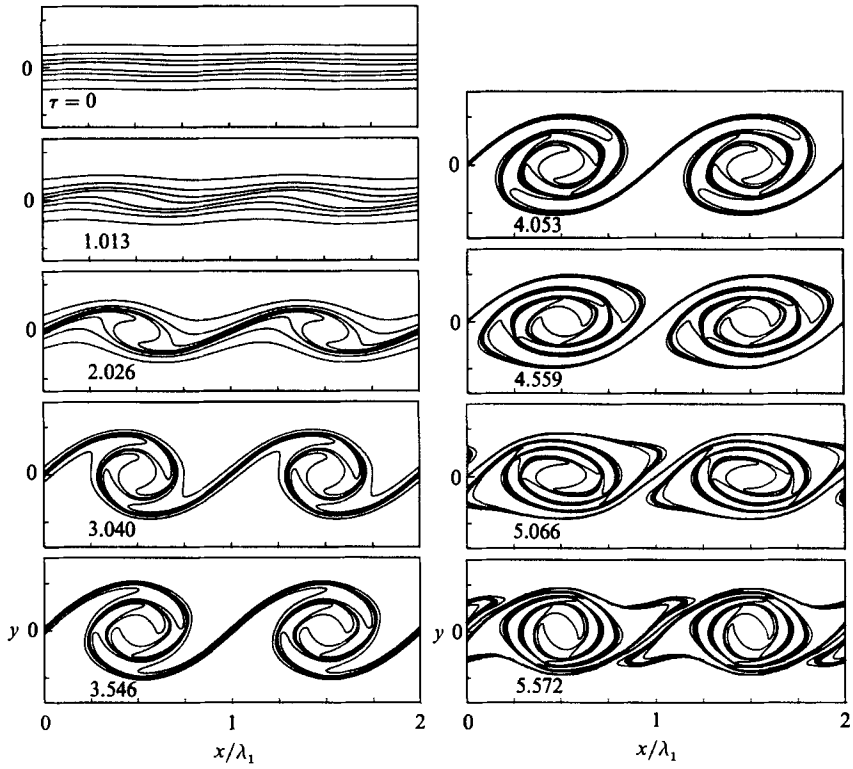

FIGURE 5. Evolution of the $M = 4$ layer disturbed by the fundamental mode perturbation, $f_1^{(4)}$ (case 3, table 3). Times τ as shown.

(iii) mean velocity profile $\langle u_x \rangle(y)$ where the spatial mean is taken over the length of the computational domain;

(iv) mean vorticity thickness of the layer δ_ω. Unfortunately δ_ω was very sensitive to the form of the velocity profile $\langle u_x \rangle$, especially near $y = 0$;

(v) mean momentum thickness of the layer

$$\theta = \int_{-\infty}^{\infty} \left[\frac{1}{4} - \left\{\frac{\langle u_x \rangle}{\Delta U}\right\}^2\right] \mathrm{d}y. \tag{15}$$

Being an integral measure, θ was less sensitive to the velocity profile $\langle u_x \rangle(y)$, and hence more suitable for comparison with experimental results;

(vi) velocity fluctuation intensities;

(vii) Reynolds stresses;

(viii) local vorticity thickness of the braid connecting the spanwise vortices

$$\delta_2 = \left[\sum_{j=1}^{M} \omega_j (h_j - h_{j+1})\right] \Big/ \omega_M, \tag{16}$$

where $h_{M+1} = 0$ and $h_j, j = 1 \ldots M$ are measured 'by hand' from enlarged plots of the solution contours.

5.1. *Nonlinear roll-up*

The evolution of a non-uniform-vorticity ($M = 4$) layer disturbed by $f_1^{(4)}$ only (case 2, table 3) is shown in figure 5. The solution has started to degrade by the final times

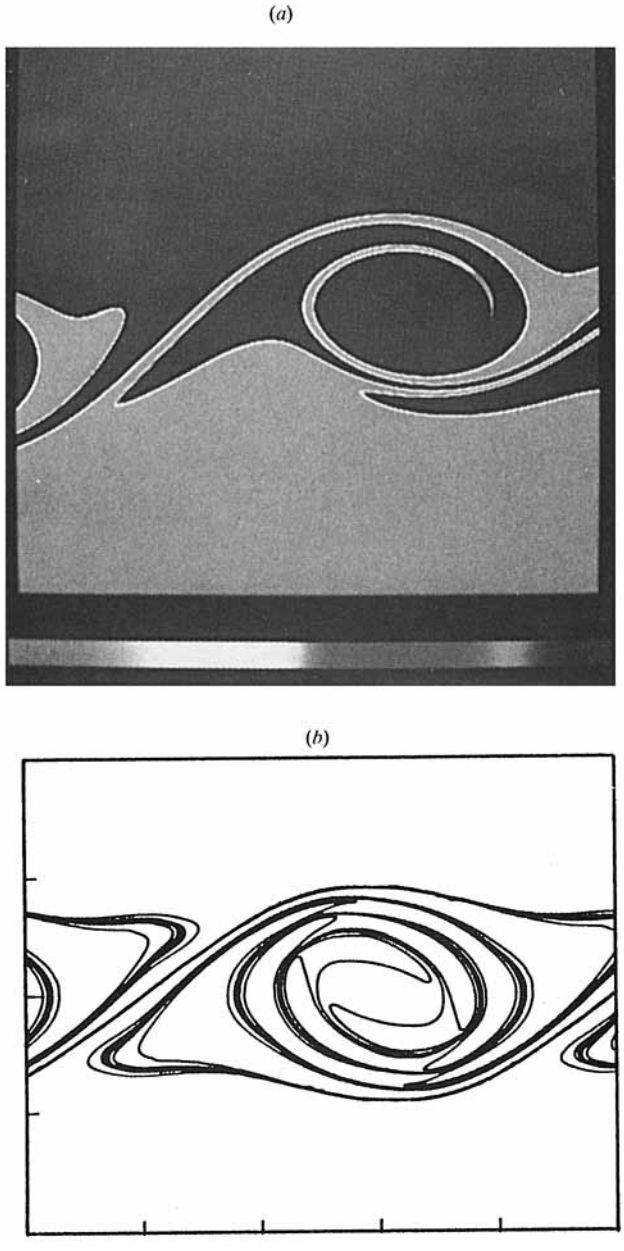

FIGURE 6. Comparison of CD solution with experimental observation. (*a*) Digital laser-induced-fluorescence picture of the plane mixing layer showing a single vortex structure, reproduced from figure 7(*a*) from Koochesfahani & Dimotakis (1986). (The original figure was in colour.) (*b*) CD solution (case 2) at $\tau = 5.284$.

shown here. By $\tau = 3.040$ most of the vorticity has been concentrated into nearly elliptical vortex cores with only a small amount of circulation left in the braids that spiral around the cores. The fluid remaining in the braids is predominantly the low-vorticity fluid. For later times, we expect that the cores will continue to rotate and deform periodically and that the braid wrapped around the cores will be stretched (in-plane) into a tightening spiral.

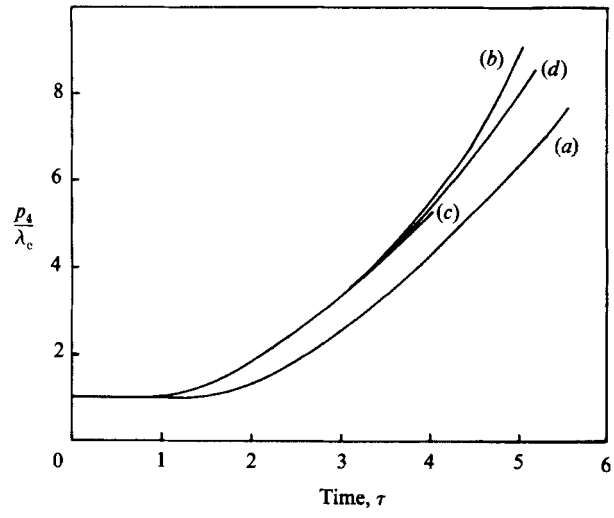

FIGURE 7. Growth of contour length, p_4, for the inner-most contour. (*a*) Single-mode roll-up (case 2); (*b*) pairing event (case 3); (*c*) tearing event (case 5); (*d*) three-vortex event (case 7).

In figure 6, we compare the $M = 4$, $\tau = 5.284$ vorticity contours and the laser-induced fluorescence (LIF) 'picture' taken by Koochesfahani & Dimotakis (1986) of a mixing layer at $Re_\delta = 1750$ (before the mixing transition). The digital LIF picture has been produced by concatenating a sequence of scans of the light intensity across the thickness of the layer as the structure was convected past the sensor. A false colour image (reproduced here in black & white) was then formed using a digital techniques. In this sense it is not an instantaneous picture of the vortical structure. Also, (i) the flow-visualization techniques rely on a passive marker to indirectly tag the vorticity field; and (ii) the experimental mixing layer possesses an asymmetry which is noticeable in figure 6(*a*). Note that we have imposed a symmetry to coordinate rotations of $n\pi$ radians in the numerical simulations by using the temporal model and a symmetric perturbation. Despite these points, there is a close similarity in features of the CD solution, the LIF picture and also the picture of the forced mixing layer taken by Roberts, Dimotakis & Roshko (1982).

It is interesting to note the migration of the vortical fluid in the braids over the adjacent vortex cores after the roll-up has occurred. In their moderate-*Re* simulations, Corcos & Sherman (1984) observed a relaxation of the vorticity distribution after a 'climax' state had been reached. This migration begins to occur at about $\tau = 5$ with the braids taking a shape similar to those in (i) the LIF picture (figure 6*a*); (ii) the vortex sheet calculations of Krasny (1986*b*, figure 13) and (iii) the initial stages of the vortex splitting process observed by Freymuth, Bank & Palmer (1984) for the accelerating flow behind an inclined aerofoil. The spiralling of the braids around the vortex cores entangles free-stream irrotational fluid in a process that we interpret as entrainment.

The interfacial area, as measured by the contour length, p_4, is shown in figure 7. Initially there is little growth in the contour length as the vorticity is concentrated into the vortex cores but, as soon as the braids are formed and begin to wrap around the cores, there is a rapid increase in the contour length. The growth rate then approaches a roughly constant value, apparently owing to the in-plane stretching of the spiral filaments around the vortex cores. These trends are similar to those

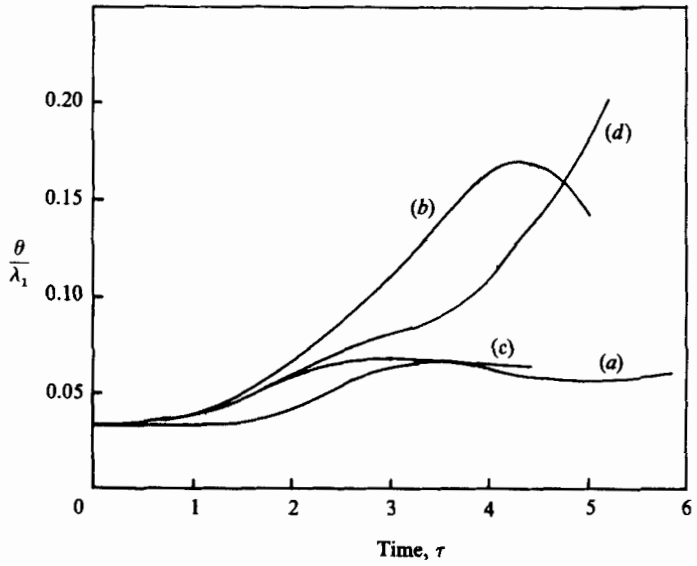

FIGURE 8. Variation in momentum thickness θ. (*a*) Single-mode roll-up (case 2); (*b*) pairing event (case 3); (*c*) tearing event (case 5); (*d*) three-vortex event (case 7).

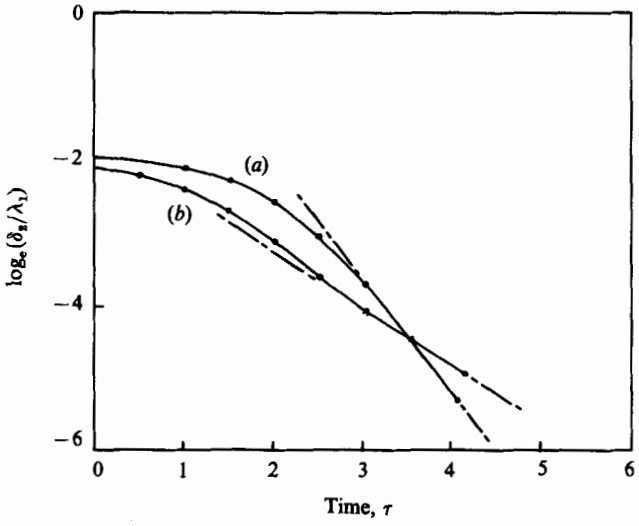

FIGURE 9. Variation of braid thickness with time. (*a*) Single-mode roll-up (case 2); (*b*) pairing event (case 3). Broken line shows prediction using strain field midway between two members of an array of equal point vortices with individual circulation Γ and spacing λ (*a*) $\lambda = \lambda_1$, $\Gamma = \Gamma_1$, (*b*) $\lambda = 2\lambda_1$, $\Gamma = 2\Gamma_1$.

observed in the numerical simulations of Pozrikidis & Higdon (1985) for the $M = 1$ layer and the water-tunnel experiments of Breidenthal (1981), although the latter experiments included a mixing enhancement due to three-dimensional motions.

In figure 8 we show the variation of momentum thickness θ with time. This plot exhibits the low-frequency fluctuations in thickness due to the 'nutation' of the nearly elliptic vortex cores, an effect first identified (and the term coined) by Zabusky

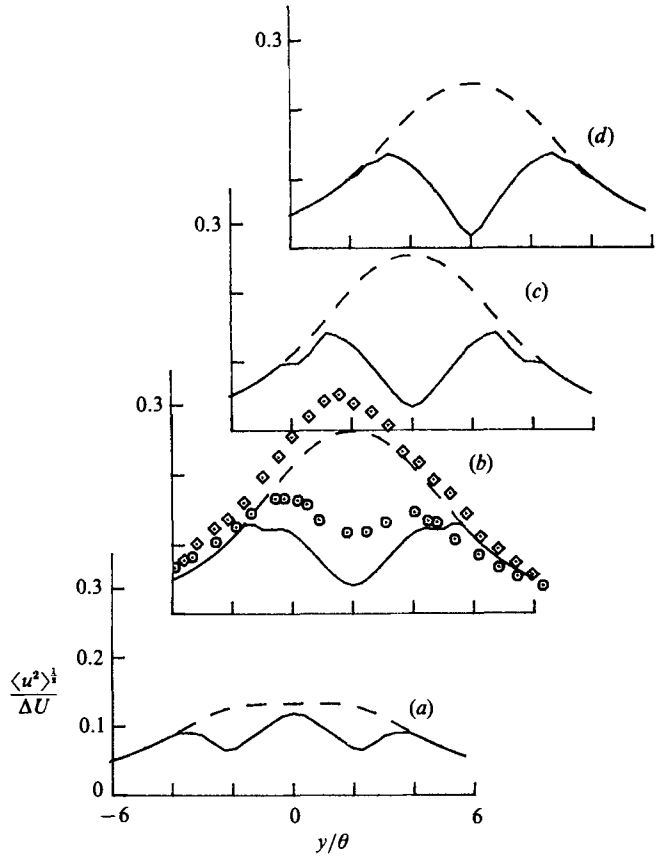

FIGURE 10. Velocity fluctuation intensities for the single-mode roll-up (case 2): ——, streamwise fluctuations $\langle u_x^2\rangle^{\frac{1}{2}}/\Delta U$; ——, transverse fluctuations $\langle u_y^2\rangle^{\frac{1}{2}}/\Delta U$. (*a*) $\tau = 2.026$; (*b*) 3.040; (*c*) 4.053; (*d*) 5.066. Symbols for experimental measurements: ⊙, streamwise fluctuations from Oster & Wygnanski (1982, figure 20), forcing frequency $f = 50$ Hz, $x = 1300$ mm; ◇, transverse fluctuations from Oster & Wygnanski (1982, figure 22), $f = 40$ Hz, $x = 1200$ mm.

& Deem (1971) in a CIC simulation of a periodic vortex street. Plots of Y_j versus time (not shown) indicate that the layer thickness reaches approximately 40%–60% of the (maximum) wavelength λ_1. This is consistent with the results of Pozrikidis & Higdon (1985).

The variation in vorticity thickness, δ_2, of the $M = 4$ braid midway between the cores is plotted on a logarithmic axis in figure 9 compared with the expected asymptotic variation of δ_2 for a model point-vortex array with vortices of strength Γ_1 and spacing λ_1. Once the vorticity layer has collapsed into compact cores (say by $\tau = 3.040$ in figure 5), the slope of the δ_2 curve approaches that of the model (i.e. $\mathrm{d}/\mathrm{d}\tau[\ln(\delta_2/\lambda_1)] = -\frac{1}{2}\pi$). The plot has been truncated at $\tau = 4.053$ owing to the difficulty in accurately measuring the braid thickness beyond this time.

In figure 10, we compare the computed velocity fluctuation intensities with the experimental measurements of Oster & Wygnanski (1982) for the forced mixing layer. We have reproduced their data for the region of the mixing layer in which there is a temporary suppression of the subharmonic interactions and we have chosen values of x and τ to demonstrate the similarity in profile features. There is a well-defined depression of the x-velocity (longitudinal) fluctuation intensity near the axis of the

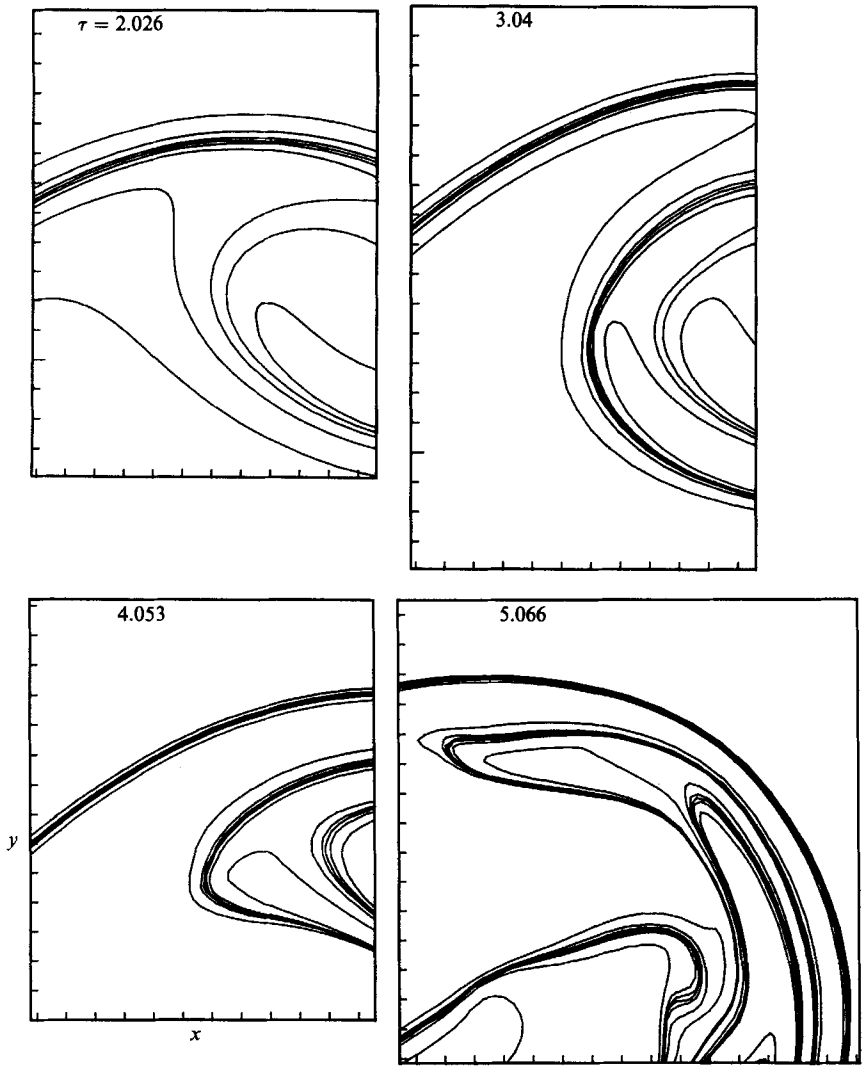

FIGURE 11. Four magnified views of the contours for the pairing calculation in figure 3 (case 3). Times τ as shown.

layer due to the close alignment of the row of vortices. Both the longitudinal and transverse fluctuations compare qualitatively with those computed for the CD simulation.

5.2. *Primary mode plus first subharmonic*

For merging of the primary vortices to occur, both the fundamental plus its subharmonic need be present. Ho & Huang (1982) have shown that, if the layer is forced by just the fundamental eigenfunction, the subharmonic is suppressed and merging delayed. Previously, Riley & Metcalfe (1980) showed that, if just the subharmonic is present, then the layer will roll-up on a larger wavelength without the merging process. Although the fundamental and subharmonic eigenfunctions may be combined with any relative phase and amplitude, we consider only the cases of table 3.

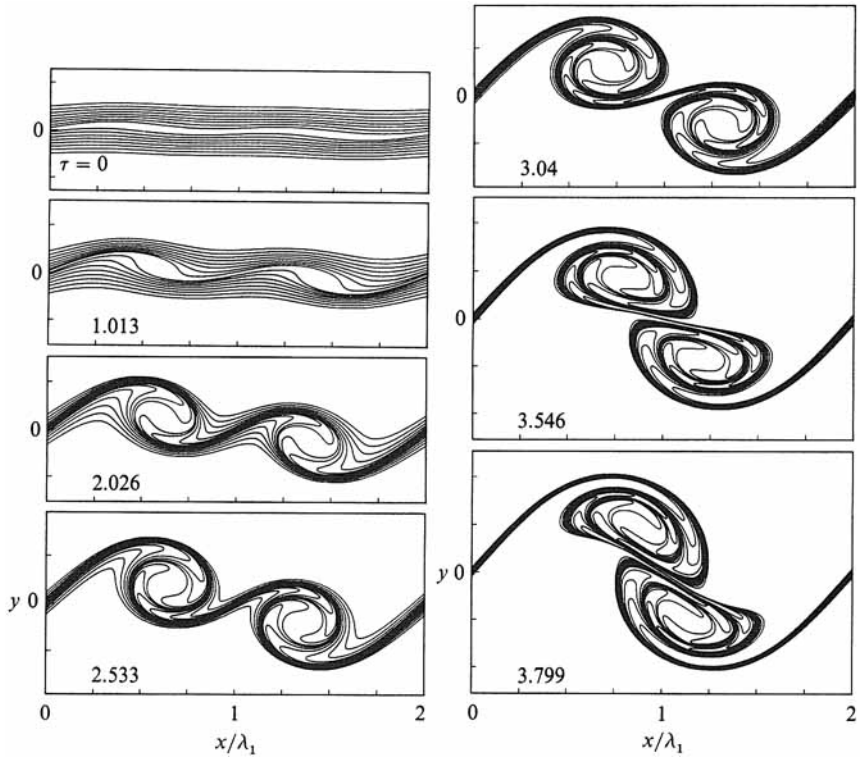

FIGURE 12. Evolution of an $M = 8$ shear layer showing a single pairing event. Initial perturbation $f_1^{(8)} + f_2^{(8)}$ (case 4, table 3). Times τ as shown.

We note that initial conditions with few harmonics are idealized; other significant harmonics will be present in experimental flows.

First we consider the evolution of the $M = 4$ non-uniform-vorticity layer with an initial perturbation defined by case 3 of table 3, with $\phi_2 = 0$. This combination of eigenfunctions leads to a pairing interaction in which two vortex cores (with initial spacing, λ_1) coalesce into a single structure. At $\tau = 0$ in figure 3 the vorticity distribution has been disturbed to produce two slight accumulations (fundamental) whose centroids have been offset from the x-axis (subharmonic). The early stage of the nonlinear roll-up is a similar process to that shown for the fundamental alone (figure 5). However, the growth of the subharmonic has become prominent by $\tau = 2.533$ with the vortex cores approaching each other and beginning to rotate about each other. By $\tau = 4.559$, the vortex cores have 'coalesced' into a single, elongated structure connected to the rest of the array (not shown) by an extremely thin braid. This braid is so fine (see for example the magnified view at $\tau = 5.066$ in figure 11) that we expect its global dynamical effect to be negligible, which may justify the use of a form contour surgery (Dritschel 1988) to remove the braids for long-time simulations. Also evident in the final two frames is the initial stage of ejection of vortex arms typical of the coalescence of two equal and otherwise isolated vortices (e.g. Christiansen & Zabusky 1973; Zabusky *et al.* 1979).

Figure 11 shows close-ups of sections of the bounding contours at four times during the evolution. The degradation of the contour smoothness is evident as τ increases

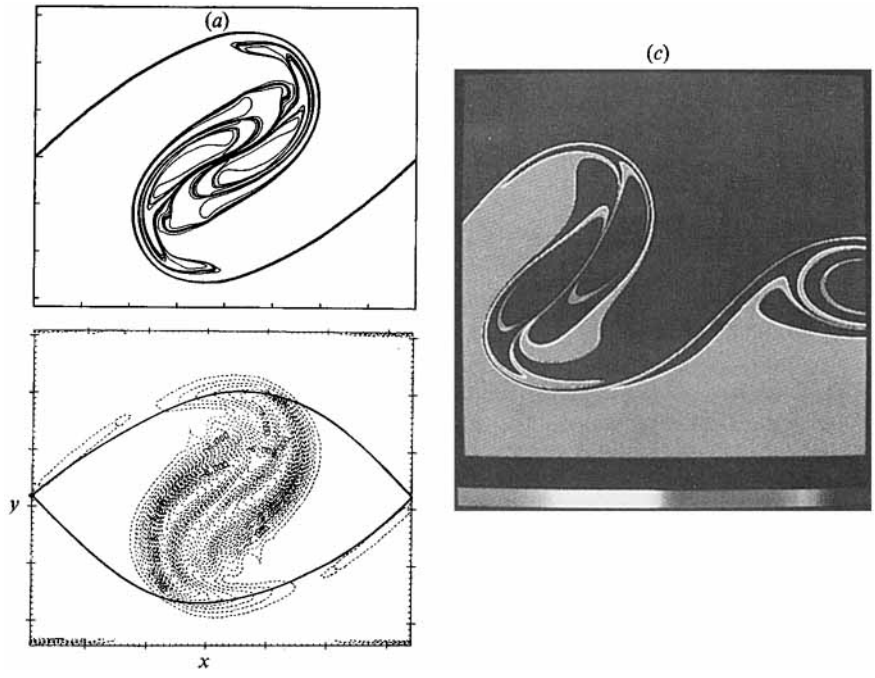

FIGURE 13. Comparison of layer evolutions involving a pairing event: (*a*) CD simulation of an invisicid shear layer at $\tau = 5.066$ (case 3, figure 3); (*b*) finite-difference calculation at $Re_\delta = 100$ reproduced from figure 8 of Corcos & Sherman (1984); (*c*) digital laser-induced-fluorescence picture of the plane mixing layer at $Re_\delta = 1750$ showing the coalescence of two vortices into a single structure, reproduced from figure 7(*b*) from Koochesfahani & Dimotakis (1986).

but, simultaneously, the detail of the vorticity distribution has increased markedly. These fine-scale features are most obvious at $\tau = 5.066$ where the contours within the vortex filaments appear to merge into a single line. Although the tracking of these vortex filaments is a computational disadvantage of the CD method, the resolution obtained in figures 3 and 11 could not be obtained with the inherently grainy vortex-element methods.

The sensitivity of the layer evolution to M is tested by performing essentially the same simulation with $M = 8$ (case 4, table 3) shown in figure 12. The initial thickness of the layer is slightly different as the maximum growth rate for $M = 8$ occurs at $k_1 \delta_\omega = 0.857$ according to the linear theory. We could not compute the evolution to the same stage as for the $M = 4$ case but, up to the time $\tau = 3.799$, the main features of the evolution are very similar. To emphasize this point we can compare corresponding $M = 4$ (figure 3) and $M = 8$ (figure 12) frames at $\tau = 3.546$. In the region between the two approaching ($M = 8$) vortex cores, the braid composed of 16 contours appears to have collapsed to a single line. Overall, the dynamics are therefore fairly insensitive to the initial vorticity profile. The braid between the pairing structures (i.e. at $x = 0$) is slightly thicker than for the $M = 4$ case but, otherwise, the intensification of vorticity gradients is essentially the same. Overlaying the figures reveals that the difference in the position of the outer contour is only approximately 1% of λ_c.

The vortex histories produced here are very similar to those generated in other numerical simulations and observed in experiments. Figure 13 shows (*a*) the

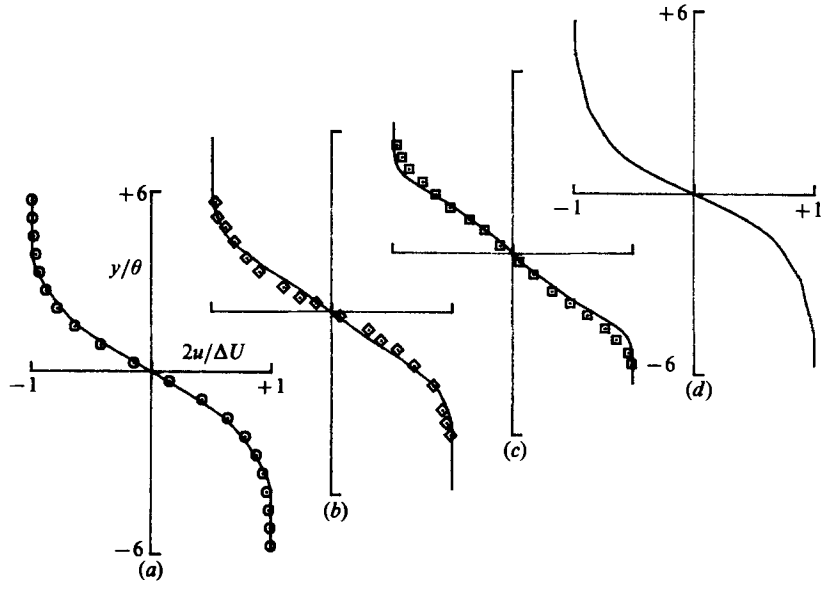

FIGURE 14. Mean velocity profiles for the pairing event. ——, computed results: (*a*) $\tau = 2.026$; (*b*) 3.040, (*c*) 4.053, (*d*) 5.066. ⊙, tanh profile; Ho & Huang (1982, figure 23) mode II mixing layer; ◇, $x = 9.5$ cm; ⊡, $x = 14.0$ cm. Note that the experimental results have been paired with the computed results to show the similarities qualitatively. They may not be at equivalent stations. Note also that the y/θ scale has been multiplied by four (◇⊡ only).

$\tau = 5.066$ frame from our $M = 4$ inviscid simulation, (*b*) the $\tau = 3.0$ frame from the $Re_\delta = O(100)$ simulation by Corcos & Sherman (1984) and (*c*) the LIF image of vortex coalescence in a plane mixing layer taken by Koochesfahani & Dimotakis (1986). The remarkably similar large-scale features in all three pictures provides supporting evidence for the hypothesis that the large-scale vortex dynamics are only weakly dependent on *Re* (Zabusky & Deem 1971).

By the final times reached in the pairing event, there seems to be less entanglement of irrotational fluid into the spiral vortex structure than for the simulations of the layer with the fundamental eigenfunction (f_1) only. This may occur because the entanglement process is relatively slow and that, as noted by Acton (1976), the pairing (and coalescence) process is very rapid, once started.

The growth of the interfacial area for the $M = 4$ layer, as measured by the contour length p_4, is shown in figure 7. The curves are very similar in form to the corresponding curve for the fundamental only except for the earlier starting time for rapid growth. (This is due to the larger initial amplitude for the fundamental eigenfunction in this pairing case.) Even in the presence of the pairing interaction, the growth of the contour length appears to be determined by the roll-up of the spiral filaments about the vortex cores.

Four representative plots of the mean velocity profile during the pairing event are shown in figure 14. There is a strong qualitative similarity in the features of these profiles and the superimposed measurements of Ho & Huang (1982) for the 'mode II' mixing layer which is forced at the first subharmonic of the most amplified frequency. Corresponding values of x and τ are chosen on the basis of similarity of profile features. The correct sequence of profiles is maintained but the increments in x may not correspond to the increments in τ. Note the difference in the measured profile at

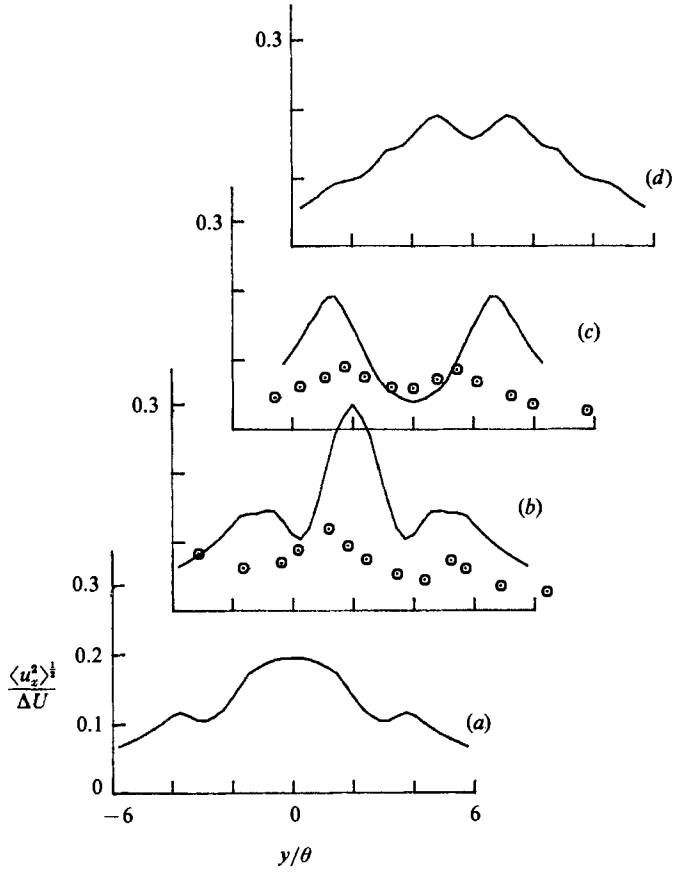

FIGURE 15. Streamwise velocity fluctuations for the pairing event (case 3) (*a*) $\tau = 2.026$, (*b*) 3.04, (*c*) 4.053, (*d*) 5.066. Symbols for experimental measurements: (*b*) Ho & Huang (1982, figure 29) mode II layer, $x = 12.0$ cm, (*c*) ibid $x = 21.5$ cm.

time $\tau = 4.053$ as the vortex centroids approach a maximum displacement from the axis of the layer. Figure 15 shows the streamwise velocity fluctuations compared with some experimental results from the mode II layer of Ho & Huang (1982). Although the comparison is quantitatively poor, both the computed and experimental data show triple- and double-peak profiles in figures 15(*b*) and 15(*c*) respectively.

The variation in calculated Reynolds stresses across the thickness of the layer is similar to the experimental measurements discussed in Ho & Huerre (1984) and the computational measurements of Aref & Siggia (1980) and Riley & Metcalfe (1980). In figure 16, we have matched the experimental profiles from Oster (1980) with our calculated results on the basis of qualitative similarity of the vortex structures (see Ho & Huerre, figure 20). The change in sign of the stresses has been explained by Ho & Huerre in terms of the orientation of the merging structure and the associated (induced) velocity field. The stresses are positive and increasing for $\tau = 2.026$, 3.04 while the velocity fluctuations are approaching a maximum but become negative for $\tau \geqslant 5$ when the merged structure passes through a 'climax' state and the velocity fluctuations begin to relax. As noted by Riley & Metcalfe (1980) this relaxation

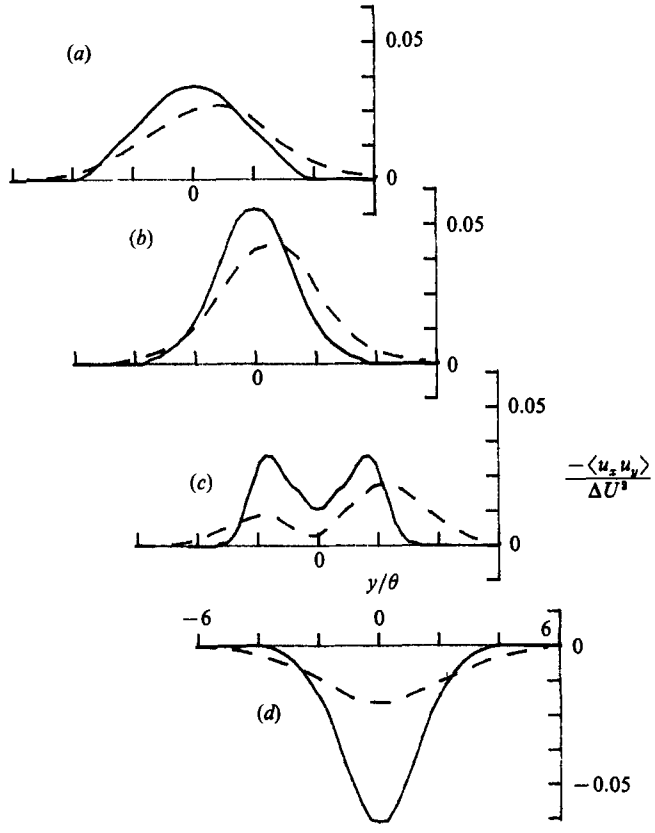

FIGURE 16. Reynolds stresses for the pairing event (case 3). ——, computed results: (*a*) $\tau = 2.026$, (*b*) 3.040, (*c*) 4.053, (*d*) 5.066. — —, measured results from Ho & Huerre (1984, figure 20) using data from Oster (1980) (*a*) $x \approx 40$ cm, (*b*) $x \approx 80$ cm, (*c*) 100 cm, (*d*) 140 cm.

produces a counter-gradient momentum flux and an associated decrease in the layer momentum thickness (figure 8*b*).

Figure 9 shows the variation of braid thickness δ_2 measured at a point on the braid midway between the coalescing structures compared with the asymptotic variation of δ_2 according to the point-vortex model with $\Gamma = 2\Gamma_1$ and $\lambda = 2\lambda_1$. Note that δ_2, here, decreases at a higher rate in $2.0 < \tau < 3.0$ owing to the stronger strain induced by the rolled-up Γ_1 vortices with an initial spacing λ_1. Beyond $\tau = 4.559$, the braid thickness was again difficult to measure owing to the degradation of the contour description.

Setting $\phi_2 = \frac{1}{2}\pi$ gives the tearing mode in which the vorticity distribution now consists of a large and a small vorticity concentration with centroids still on the x-axis. Figure 4 (case 5, table 3) shows the evolution of the layer initially with this distribution. The vorticity from the braid region is now unequally shared in the early stages of roll-up resulting in two vortex cores with significantly different strengths (circulations). The evolutionary process is similar to the 'shredding interaction' described by Patnaik *et al.* (1976). The large vortex has $1.2\Gamma_1$ while the smaller core has $0.8\Gamma_1$, where Γ_1 is the nominal circulation of a primary vortex. By the final time shown in figure 4, the processes of roll-up combined with tearing appear to be

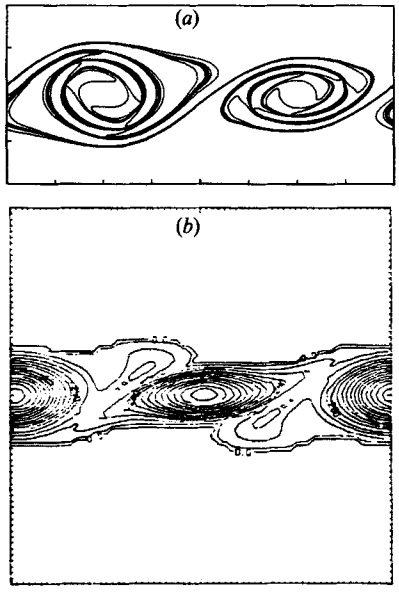

FIGURE 17. Comparison of the CD calculation (tearing mode, case 5) with a calculation at $Re = 400$. (a) $\tau = 4.433$ solution from case 5 (figure 4); (b) spectral method solution at $t = 24$ reproduced from Riley & Metcalfe (1980), figure 14(c).

complete and the vortical fluid accumulated by the larger core in thick filaments (near the core) is beginning to migrate away and over the top of the smaller vortex core.

The inviscid tearing simulation has different long-time behaviour to the moderate-Re simulations of Riley & Metcalfe (1980). Although their simulation at $t = 24$ has a very similar vorticity distribution to the CD solutions at $\tau = 4.433$ (see figure 17) they suggest (but did not show in their figures) that the fluid from smaller vortex will eventually be redistributed into the larger cores. However, our inviscid simulations suggest that the smaller core is now stable to the tearing instability, which lends support to the conjecture by Moore & Staffman (1975) that the tearing process requires viscous diffusion to proceed to completion. The layer's evolution is now similar to the simulation containing the fundamental only. The growth of layer thickness as measured by the momentum thickness (figure 8) and the growth of contour length p_j (figure 7) closely resemble the corresponding curves for the single-mode calculation.

For any relative phase $0 < \phi_2 \leqslant \frac{1}{2}\pi$ the disturbance may be decomposed into a pairing component and a tearing component. Pairing is the stronger of these two effects (Acton 1976; Riley & Metcalfe 1980; Corcos & Sherman 1984) and so, when there is a random combination, we expect the pairing process to occur most frequently, as observed by Hernan & Jimenez (1982). We computed the evolution of a layer with $\phi_2 = \frac{1}{4}\pi$ (case 6, table 3). Initially, tearing produces two unequal vortex cores which at later times approach each other and coalesce into a single structure in much the same way as the pure pairing case (case 3, figure 3).

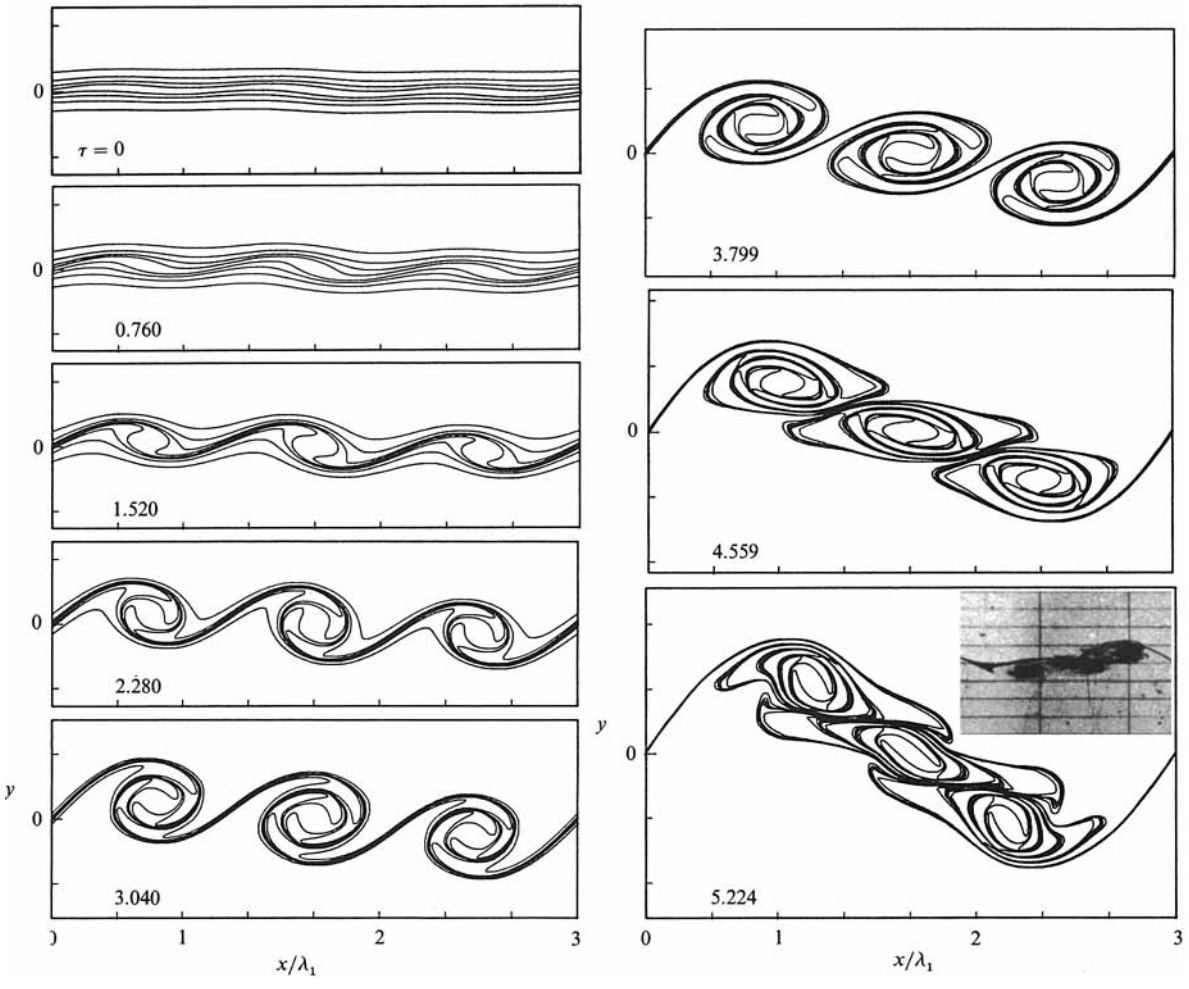

FIGURE 18. Evolution of an $M = 4$ layer showing a three-vortex coalescence. Initial disturbance $f_1^{(4)} + f_3^{(4)}$ (case 7, table 3). Inset on the solution at $\tau = 5.224$ is a reproduction of part of figure 6(a) ($x = 21.0$) from Winant & Browand (1974). Note that the shear across the layer is in the opposite sense.

5.3. *Primary mode plus second subharmonic*

The next level of complexity in the interaction of subharmonics is the three-vortex event. We consider the evolution of the two-dimensional shear layer with an initial condition defined by case 7 of table 3. The computational domain now contains three wavelengths of the fundamental eigenfunction. Figure 18 shows the layer evolution until a time of $\tau = 5.224$. Initially the layer rolls into characteristic cores and, as the subharmonic grows, the two outer cores begin to rotate about and approach the central core. By the final times shown, the vortex cores have merged into a single elongated structure which contains much fine-scale detail, especially in the regions where the braids interact with vortex cores. Inset in the last frames is a section of a photograph taken by Winant & Browand (1974) showing a three-vortex structure which is very similar to that produced in our numerical simulation (except that the shear direction is reversed). Figure 19a is a close-up of one of the outer vortex cores at $\tau = 5.224$. The braids have become extremely thin in places but have still

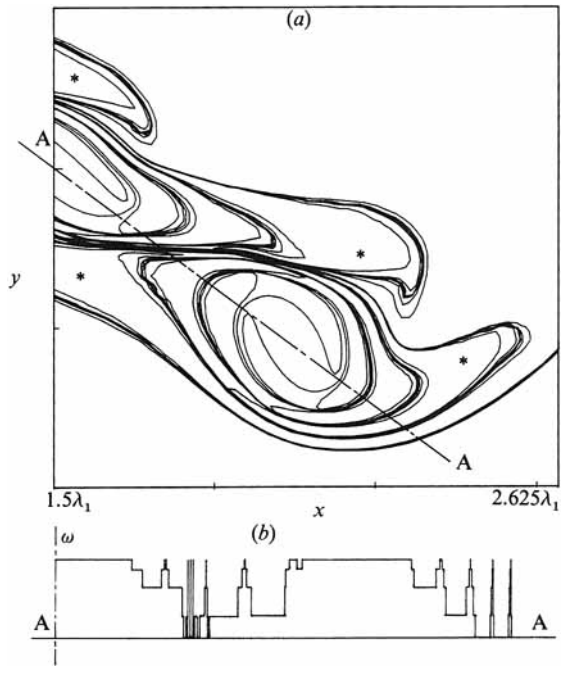

FIGURE 19. (*a*) Magnified view of the vortex contours for case 7 (figure 18) at $\tau = 5.224$. Tic-mark spacing is $3\lambda_1/8$. * denotes irrotational fluid. (*b*) Vorticity profile along the section AA.

maintained their coherence although the contour smoothness has started to degrade. The complexity of the vorticity distribution is illustrated in figure 19*b* which is a vorticity profile along the section through the three vortex cores. Four close-ups of the contour evolution are contained in figure 20. As τ increases the contour description degrades more quickly than for case 3 (figure 11).

The growth of the interfacial area with time (see figure 7) is almost identical with those from the two-vortex pairing up until $\tau = 4.0$ with rapid growth commencing as soon as the braids were formed. The growth of the layer thickness is again shown by the momentum thickness, θ, in figure 8. As would be expected from inspection of the vorticity distribution in figure 18, the evolution is still in the rapid growth region before the structure reaches its climax. (The axis joining the vortex centroids is not yet aligned with the cross-stream direction.) We expect that, if the simulation was continued, θ would eventually reach a plateau and then relax. We did not have sufficient computing resource to test this hypothesis.

6. Stretched shear layers

6.1. *Models of the streamwise vorticity*

We now consider the evolution of prototype structures for the streamwise vorticity superimposed upon the quasi-two-dimensional base flow of spanwise vortices. We use the Corcos–Lin model of streamwise vortices as a starting point. For this model the secondary vortices are assumed to consist of an array of highly flattened, ribbon-like vortices with alternating circulations of magnitude Γ_2 and spanwise spacing λ_2 where the subscript now refers to the jth tier of the CLS model. Experimental measurements (e.g. Jimenez 1983) indicate that $\Gamma_2 \approx \beta\Gamma_1$ where $\beta = O(1)$ and $\lambda_2 \approx \lambda_1$. Locally, the

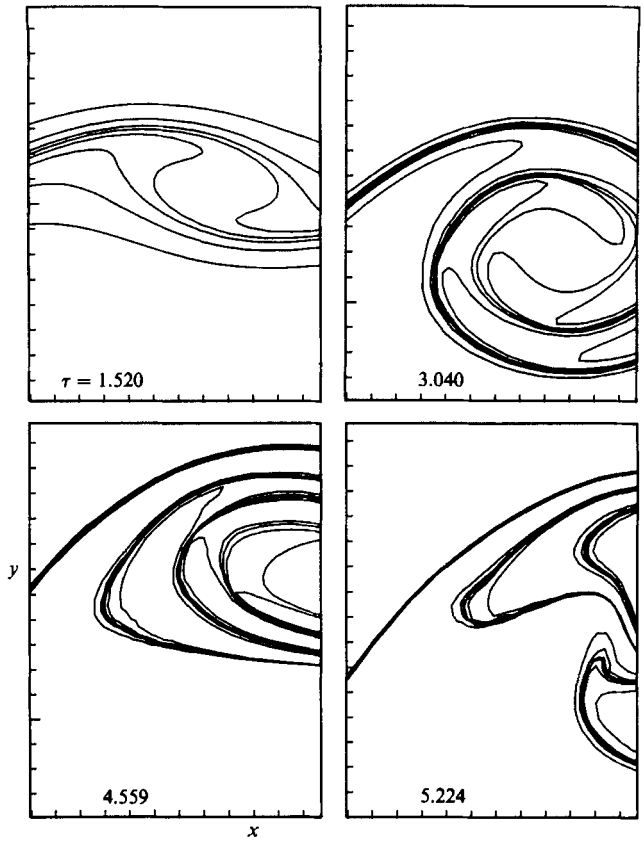

FIGURE 20. Four magnified views of the contours in case 7 (figure 18). Times τ as shown; tick-mark spacing = $3\lambda_1/20\pi$.

vortices are aligned with the braid and evolve in the ambient three-dimensional stretching strain field provided by the primary (spanwise) vortices. The inviscid secondary vortex simulations of Pullin & Jacobs (1986) (especially those with high aspect ratios) show secondary vortices evolving rapidly into a string of compact vortex cores connected by braids of streamwise vorticity. An example is shown in figure 21 with (in their notation) $M = 4$, the vortex aspect ratio $a_2 = 51.7$, and the dimensionless stretching strain rate $\hat{\gamma}_2 = \gamma_2 \lambda_2^2/(4\pi^2 \Gamma_2)$ has the value $\hat{\gamma}_2 = 0.1$. Locally, that is within the dashed box of figure 21, the evolution is qualitatively similar to the purely two-dimensional roll-up of the primary (or spanwise) vortices. These small-scale vortices, which we associate with the tertiary motions of the CLS model, evolve in the ambient strain environment provided by the primary vortices. Given the similarities with the two-dimensional-layer evolution, it appears profitable to study the behaviour of a stretched shear layer as a model of the secondary vortices in the limit of $a_2 \to \infty$.

The stretched shear layer has been studied by Lin & Corcos (1984) at moderate Re_δ using a finite-difference technique. They used a Burgers' vortex layer as an initial condition and found roll-up and, in some cases, pairing similar to that for the purely two-dimensional layer but substantially modified by the ambient strain environment. Note that, unlike the viscous simulations of Lin & Corcos (1984), the undisturbed $Re = \infty$ flow here has no equilibrium state (the initially unperturbed

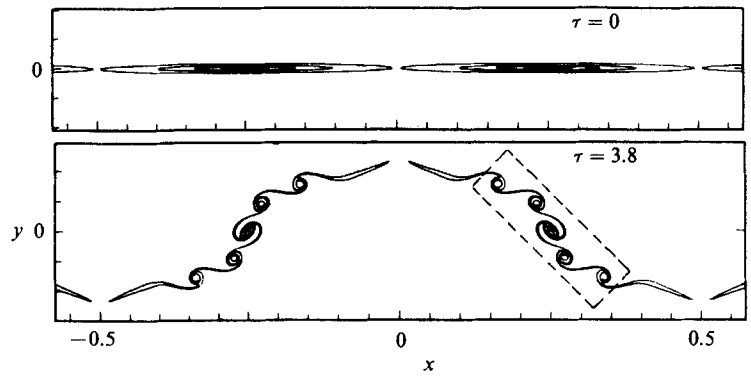

FIGURE 21. Initial and final solution frames for the evolution of the secondary vortex array, $a_2 = 51.7$, $\hat{\gamma}_2 = 0.1$ (Pullin & Jacobs 1986). The dashed box denotes the region where the vortex dynamics appears qualitatively similar to that for a periodic layer.

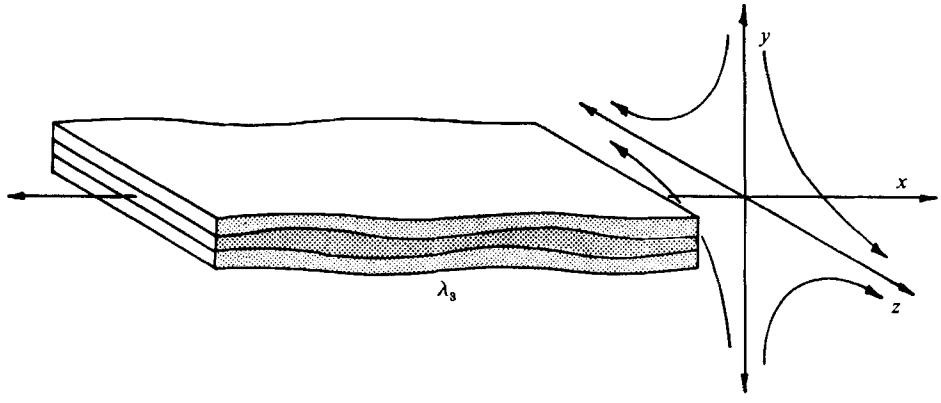

FIGURE 22. A section of an x-periodic shear layer subject to locally uniform three-dimensional strain. The layer shown here consists of three regions of uniform vorticity ω.

layer decreases monotonically in thickness as $\exp(-\gamma t)$). In the present simulations, we effectively 'turn on' the dynamics at $t = 0$.

In figure 22 we show a conceptual view of the prototype flow model. A non-uniform unidirectional vorticity profile is approximated by a piecewise-constant distribution in the same way as for the purely two-dimensional layer. The imposed stretching strain (4) is represented by the four streamline segments in the (y, z)-plane. The layer is periodic in the (spanwise) x-direction and the extensional axis of the strain is aligned with the vortex lines along the z-axis (i.e. parallel to the braids in the primary motion). The circulation contained in one wavelength λ_3 of the rolled-up vortex cores is Γ_3, giving $\Delta U_3 = \Gamma_3/\lambda_3$ as the velocity jump across the layer. Here, we choose the stretching strain parameter γ_3 to model conditions which prevail locally within the dashed box depicted in figure 21. For this purpose we approximate $\lambda_3 \approx 0.075\lambda_2$ and $\Gamma_3 \approx 0.15\Gamma_2$. Using a lengthscale $L = \lambda_3$ and a timescale $T = \lambda_3^2/\Gamma_3$, the local dimensionless strain rate $\hat{\gamma}_3 = \gamma_3 T$ is then given roughly by $\hat{\gamma}_3 = 1.5\hat{\gamma}_2$. Thus, values of $\hat{\gamma}_3 = 0.15$ and $\hat{\gamma}_3 = 0.30$ were selected in order to study qualitatively the trends with finite $\hat{\gamma}_3$. For discussion we put $\tau = t/T$.

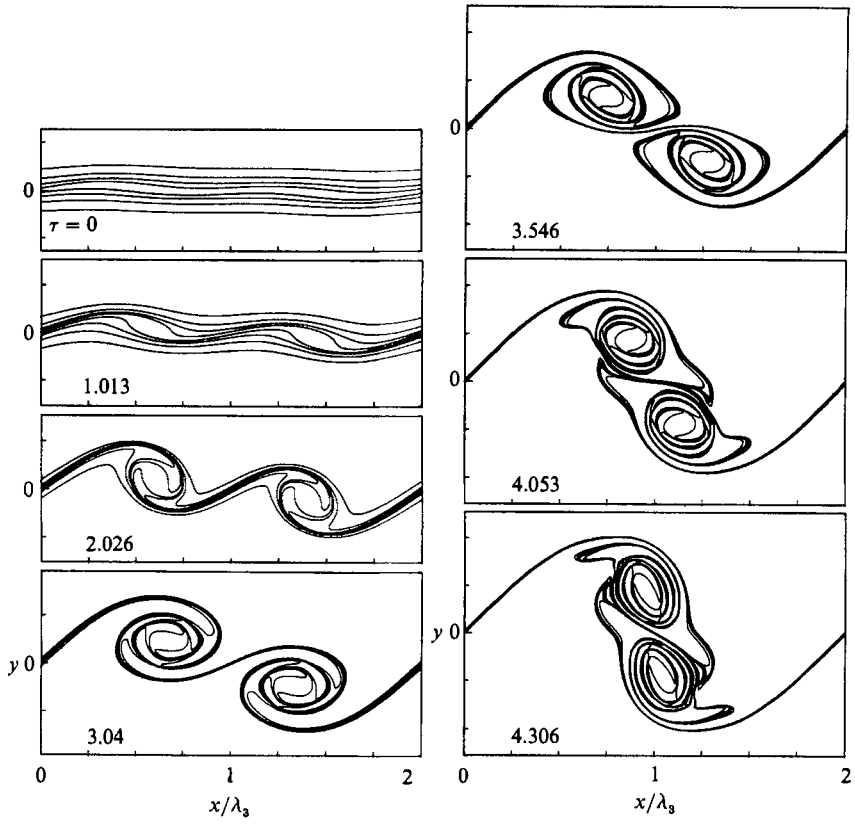

FIGURE 23. Evolution of a stretched shear layer showing a single pairing event, $\hat{\gamma}_3 = 0.15$, $k_3\delta_\omega = 0.875$, $k_3\alpha_1 = 0.10$, initial disturbance f_1+f_2 (case 1, table 3). Times τ as shown.

6.2. *Discussion*

Figure 23 shows the evolution of a stretched layer initially perturbed as in case 3 of table 3, while figure 24 compares the contour profiles at a similar stage of evolution for $\hat{\gamma}_3 = 0$, 0.15 and 0.30. When $\hat{\gamma}_3 > 0$ the intensification of vorticity combined with the conservation of circulation leads to a reduction in the area enclosed by the bounding contours. Also it accelerates the roll-up into compact cores and enhances the production of the spiral filaments that wind around these cores. Figure 25 shows the variation of contour lengths with time. Once the spiral filaments have formed, there is a rapid increase in the contour length, as occurred in the two-dimensional simulations. Howwever, the stretching induces a higher rate of growth. For the higher strain rate ($\hat{\gamma}_3 = 0.30$), these effects are more pronounced. At $\tau = 3.5$ in the pairing simulations, $p_4/\lambda_c = 2.6$, 3.2 and 4.0 for $\hat{\gamma}_3 = 0$, 0.15, 0.30 respectively.

The stretching strain also has a marked effect upon the interaction of the subharmonic. First, it inhibits the rotation of the centroids of the vortex cores about each other and, secondly, the reduction in area of the vortex cores inhibits coalescence of the rolled-up cores. More evidence for the inhibition of rotation of the centroids is contained in figure 26, which shows that, for any particular time, the maximum height reached is reduced with increasing strain. For example, at $\tau = 3.5$, $Y_1/\lambda_1 = 0.468$, 0.40, 0.352 with $\hat{\gamma}_3 = 0$, 0.15, 0.30 respectively. However, in both plots having $\hat{\gamma}_3 > 0$, Y_1 still has a high growth rate at the final times shown. The

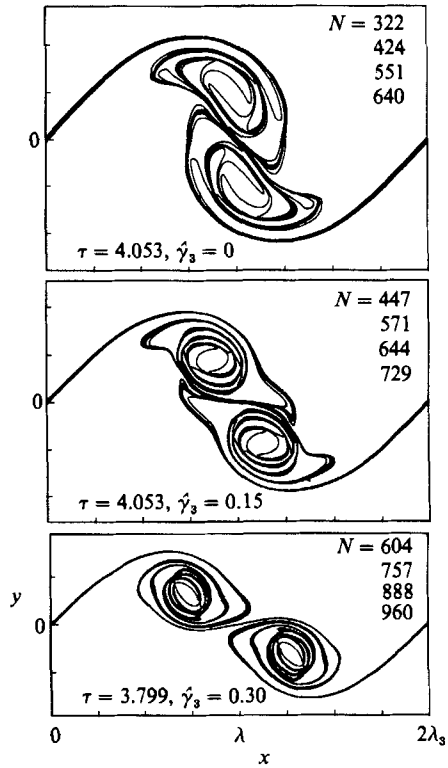

FIGURE 24. Comparison of late-time solutions for the pairing event with 3 values of stretching, $\hat{\gamma}_3$. Times τ stretching strain strength $\hat{\gamma}_3$ and numbers of nodes N defining C_j, $j = 1 \ldots 4$ as shown.

extent to which the pairing interaction is inhibited may be explained by decomposing the (y, z)-plane strain field into an axisymmetric component

$$\boldsymbol{u}_{\mathrm{a}} = -\tfrac{1}{2}\gamma_3(x\boldsymbol{i}+y\boldsymbol{j})+\gamma_3 z\boldsymbol{k}. \tag{17}$$

and an (x, y)-plane component

$$\boldsymbol{u}_{\mathrm{2d}} = \tfrac{1}{2}\gamma_3(x\boldsymbol{i}-y\boldsymbol{j}), \tag{18}$$

where $\boldsymbol{u}_{\mathrm{s}} = \boldsymbol{u}_{\mathrm{a}}+\boldsymbol{u}_{\mathrm{2d}}$, and then transforming to an equivalent two-dimensional (x, y)-plane flow (Lundgren 1982) with time variable t' given by

$$t' = \int_0^t \exp[Q(t'')]\,\mathrm{d}t''. \tag{19}$$

With the line joining the vortex centroids nearly aligned with the x-axis, the (x, y)-plane strain,

$$\boldsymbol{u}_{\mathrm{s}} = \tfrac{1}{2}\gamma_3 \exp[-Q(t(t'))]\,(x\boldsymbol{i}-y\boldsymbol{i}), \tag{20}$$

in the equivalent two-dimensional flow tends to separate the vortex cores thus slowing and/or inhibiting the tendency for the cores to merge (Jacobs & Pullin 1985). In the stretched-layer simulations, however, the velocity vector (consisting of the stretching strain plus the induced field due to the rest of the vortex array) at the centroid of a vortex core includes a component towards the centre of symmetry of the vortex pair (Lin & Corcos 1984). Thus, although the pairing process may be

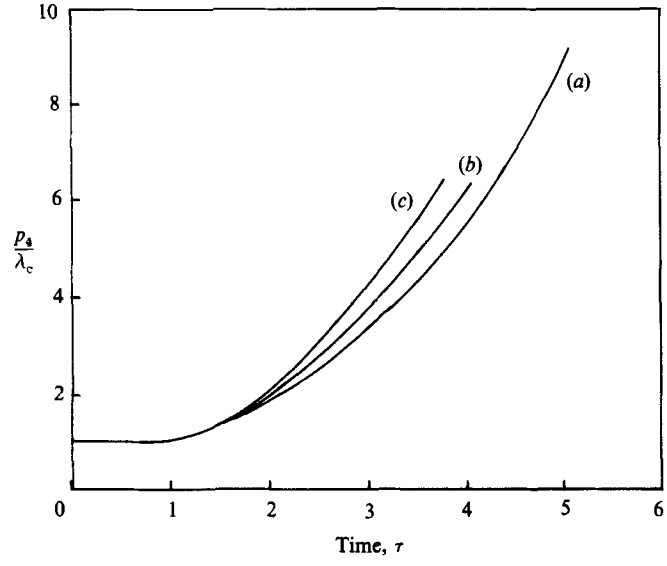

FIGURE 25. Growth of contour length, p_4, for the innermost contour for the pairing event with stretching; (*a*) $\hat{\gamma}_3 = 0$, (*b*) 0.15, (*c*) 0.30.

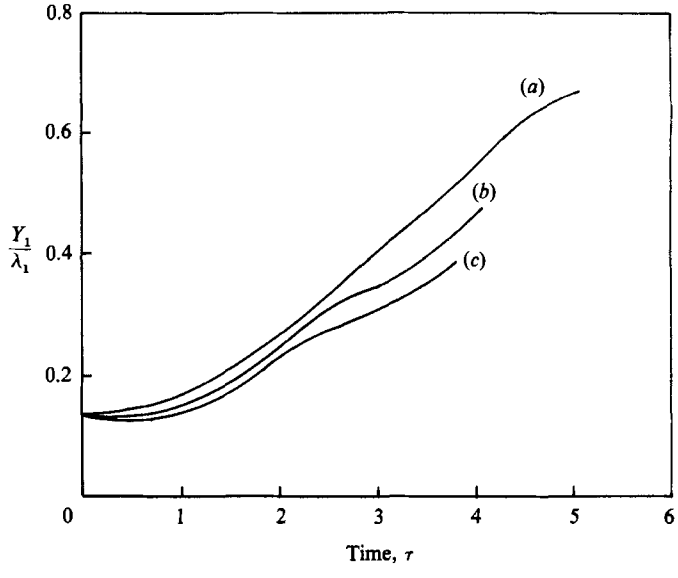

FIGURE 26. Variation of maximum contour height, Y_1 for the outermost contour for the pairing event with stretching: (*a*) $\hat{\gamma}_3 = 0$, (*b*) 0.15, (*c*) 0.30.

initially inhibited, the stretched vortices will always approach each other if they are initially perturbed in an alternating fashion.

Two simulations involving the pure-tearing interaction were also performed for $\hat{\gamma}_3 = 0.15$ and 0.30 respectively (not shown presently). Again the vorticity intensification leads to increased speed of rotation of the cores and enhanced production of spiral filaments but the effect on the tearing interaction appears to be minimal. For both values of stretching investigated, the tearing interaction

proceeded to a point where the larger vortex circulation was 1.5 times that of the smaller vortex, in much the same time as for the $\hat{\gamma}_3 = 0$ case. Another feature inhibited by vortex stretching is the migration of the thick braid formed around the larger core. In the relatively long-time $\hat{\gamma}_3 = 0$, simulations of the single-mode perturbation (case 2, table 3), the fluid contained in the braids migrated along the layer. However, for the finite $\hat{\gamma}_3$ here, the spiral filaments are rapidly tightened about the concentrated cores and do not migrate.

7. Conclusions

We have applied the CD method to the vortex modelling of various eddy scales relevant to the plane turbulent mixing layer at the nominal limit of $Re = \infty$, for moderate times. For the strictly two-dimensional temporal instability and roll-up of the plane shear layer, we examined the influence of the initial vorticity profile and the presence of various subharmonic disturbances on the layer evolution. In all cases, the inviscid simulations led to the production of much fine-scale detail, which usually resulted in termination of the computation.

Overall, the simulations showed that variations in the initial vorticity field had only a minor effect on the flow evolution but that the subharmonic content of the initial perturbation greatly influenced the post-rolled-up evolution. Disturbing the layer with a perturbation consisting of a combination of the fundamental eigenfunction and its first subharmonic resulted in a range of post-rolled-up evolutions for differing values of phase angle ϕ_2. For $\phi_2 = 0$, adjacent vortex pairs rotated about each other and coalesced into an array of larger vortical structures with a larger wavelength. Comparisons with finite-Re simulations and experimental observations provide supporting evidence for the hypothesis that the large-scale vortex dynamics for the roll-up and pairing processes are only weakly dependent upon Re (Zabusky & Deem 1971). Setting $\phi_2 = \frac{1}{2}\pi$ resulted in a tearing interaction in which the roll-up of the layer produces adjacent vortex cores of different strengths. Unlike previous moderate-Re simulations, the smaller cores produced in the $Re = \infty$ simulation here were not completely absorbed by the larger vortices on either side. Disturbing the layer with a combination of the fundamental eigenfunction and its second subharmonic resulted in the roll-up and subsequent interaction of subsets of three adjacent vortices in a manner similar to that observed in the forced mixing-layer experiments of Ho & Huang (1982).

The stretching-strain/vortical interaction studied in the secondary vortex and stretched-layer simulations provided an example of an energy transfer mechanism (relevant to the turbulent energy cascade) from the large-scale motions (plane strain field) to the smaller-scale vortex motions. The evolution of the stretched vortex layer was not explored in depth but the calculations performed indicated some of the effects of stretching. In particular, the stretching enhanced the production of spiral filaments but inhibited the coalescence of the rolled-up vortex cores for the pairing simulations. A feature not included in the calculations but evident in the experimental flow-visualization pictures is the presence of strong random per-tubratons (see e.g. Roshko 1980) and fully three-dimensional instabilities. The relevance of the stretched-shear-layer calculations is questionable as these instabilities may destroy the flow coherence on a time-scale comparable with that found for the evolution of the fine structure in either the primary or higher-order vortex simulations.

Part of this work was supported by the Australian Research Grants Scheme under grant No. F8315013 I. P.A.J. was supported by an Australian Commonwealth Postgraduate Research Award. Computing time was given by the CSIRO. on their Cyber 205.

Appendix: Analytic-patch procedure

For small $|\zeta-\zeta'|$ and ζ not on the contour, the accuracy of the velocity calculation is improved by the application of an 'analytic-patch' procedure. The full integrand in (7) has the form (with $\lambda_c = 2\pi$)

$$I_{\text{total}} = (y-y')\cot[\tfrac{1}{2}(\zeta-\zeta')]\frac{\mathrm{d}\zeta'}{\mathrm{d}e'}, \tag{A 1}$$

which, for small $|\zeta-\zeta'|$, may be expanded. Retaining only first-order terms, this integrand can be approximated by

$$I_{\text{fast}} = 2\frac{(y-y')}{(\zeta-\zeta')}\frac{\mathrm{d}\zeta'}{\mathrm{d}e'}. \tag{A 2}$$

For segments on which the full integrand (A 1) is well behaved (i.e. slowly varying), we numerically integrate I_{total} but, on segments where our fixed quadrature is inaccurate owing to rapid variations of this integrand, we integrate

$$I_{\text{slow}} = \left\{(y-y')\cot[\tfrac{1}{2}(\zeta-\zeta')]-2\frac{(y-y')}{(\zeta-\zeta')}\right\}\frac{\mathrm{d}\zeta'}{\mathrm{d}e'}, \tag{A 3}$$

and add the analytically derived value for I_{fast}. This 'analytic-patch' procedure is implemented on segments for which

$$\min(|(\zeta_j)_k-\zeta_m(e_i)|, \mathrm{i} = 0\ldots3) < \text{segsize}, \tag{A 4a}$$

$$\text{segsize} = |(\zeta_m)_{n+1}-(\zeta_m)_n|+|(\zeta_m)_n-(\zeta_m)_{n-1}|, \tag{A 4b}$$

and $(\zeta_j)_k \neq \zeta_m(e)$, $-1 \leqslant e \leqslant 1$ (i.e. $(\zeta_j)_k$ is not part of C_m). A check is also made for the images of the velocity point in the wavelengths either side of the computational domain, $(\zeta_j)_k \pm 2\pi$. This criterion was derived from empirical results contained in Jacobs (1987). Although the check on proximity (A 4) is fairly crude, it is still too expensive to compute each time the velocity routine is called. We assume that the nodes do not move too far between calls to the node-adjustment routine and so, on entry to the velocity routine for the first time with a new set of nodes, we store an index of the 'close' segments (i.e. those that satisfy equation A 4) for each node. This information is stored in a large integer 'index-array'. After summing the numerically integrated contributions of each segment to the velocity of a particular node, we then look up the 'index-array' and adjust the contribution of the 'close' segments that are listed for this node.

When the 'analytic-patch' is to be used, we calculate the value of I_{fast} using either two straight lines approximating the segment (if $|A| < \epsilon$, $\epsilon \approx 10 \times$ machine precision) or the parabolic segment. The expressions for the straight-line segments are very similar to those in Jacobs (1987), while the expressions for the parabolic segment are

$$\int_{-1}^{1} \tfrac{1}{2} I_{\text{fast}}\,\mathrm{d}e = T_1 + A_2 T_2 + A_3 T_3, \tag{A 5a}$$

where

$$T_1 = 2(2B_I - A_I B/A), \tag{A 5b}$$

$$A_2 = -T_I + [A_I T + \tfrac{1}{2}B(-B_I + A_I B/A)]/A, \tag{A 5c}$$

$$T_2 = \ln[(\zeta_j)_k - (\zeta_m)_{n+1}] - \ln[(\zeta_j)_k - (\zeta_m)_{n-1}], \tag{A 5d}$$

$$A_3 = -2B_I T + [2A_I T + \tfrac{1}{2}B(-B_I + A_I B/A)]B/A, \tag{A 5e}$$

$$T_3 = \frac{1}{(-\Delta)^{\frac{1}{2}}}\left\{\ln\left[\frac{-B-2A-(-\Delta)^{\frac{1}{2}}}{-B-2A+(-\Delta)^{\frac{1}{2}}}\right] - \ln\left[\frac{-B+2A-(-\Delta)^{\frac{1}{2}}}{-B+2A+(-\Delta)^{\frac{1}{2}}}\right]\right\}, \tag{A 5f}$$

and where

$$(-\Delta) = (B^2 + 4AT), \tag{A 5g}$$

$$T = (\zeta_j)_k - (\zeta_m)_n, \tag{A 5h}$$

$$A = \tfrac{1}{2}((\zeta_m)_{n+1} - 2(\zeta_m)_n + (\zeta_m)_{n-1}), \tag{A 5i}$$

$$B = \tfrac{1}{2}((\zeta_m)_{n+1} - (\zeta_m)_{n-1}). \tag{A 5j}$$

The subscript I indicates the imaginary part. A derivation of these expressions along with a description of the logic required to select the correct log branches of T_2 and T_3 is contained in Jacobs (1987).

REFERENCES

Acton, E. 1976 The modelling of large eddies in a two-dimensional shear layer. *J. Fluid Mech.* **76**, 561–592.

Aref, H. 1983 Integrable, chaotic, and turbulent vortex motion in two-dimensional flows. *Ann. Rev. Fluid Mech.* **15**, 345–389.

Aref, H. & Siggia, E. D. 1980 Vortex dynamics of the two-dimensional turbulent shear layer. *J. Fluid Mech.* **100**, 705–737.

Ashurst, W. T. 1977 Numerical simulation of turbulent mixing layers via vortex dynamics. In *Turbulent Shear Flows I* (ed. by F. Durst *et al.*) pp. 402–413. Springer.

Breidenthal, R. 1981 Structure in turbulent mixing layers and wakes using a chemical reaction. *J. Fluid Mech.* **109**, 1–24.

Browand, F. K. & Weidman, P. D. 1976 Large scales in the developing mixing layer. *J. Fluid Mech.* **76**, 127–144.

Christiansen, J. P. & Zabusky, N. J. 1973 Instability, coalescence and fission of finite-area vortex structures. *J. Fluid Mech.* **61**, 219–243.

Corcos, G. M. & Lin, S. J. 1984 The mixing layer: deterministic models of a turbulent flow. Part 2. The origin of the three-dimensional motion. *J. Fluid Mech.* **139**, 67–95.

Corcos, G. M. & Sherman, F. S. 1984 The mixing layer: deterministic models of a turbulent flow. Part 1. Introduction and the two-dimensional flow. *J. Fluid Mech.* **139**, 29–65.

Damms, S. M. & Kuchemann, D. 1974 On a vortex-sheet model for the mixing between two parallel streams. I. Description of the model and experimental evidence. *Proc. R. Soc. Lond.* A **339**, 451–461.

Dritschel, D. G. 1986 The nonlinear evolution of rotating configurations of uniform vorticity. *J. Fluid Mech.* **172**, 157–182.

Dritschel, D. G. 1987 The repeated filamentation of vorticity interfaces. *IUTAM Symposium on Fundamental Aspects of Vortex Motion, Tokyo, Japan.*

Dritschel, D. G. 1988 Contour surgery: A topological reconnection scheme for extended integrations using contour dynamics. *J. Comput. Phys.* **77**, 240–266.

Forsythe, G. E., Malcolm, M. A. & Moler, C. B. 1977 Computer methods for mathematical computations. Prentice Hall.

FREYMUTH, P., BANK, W. & PALMER, M. 1984 First experimental evidence of vortex splitting. *Phys. Fluids* **27**, 1045–1046.

HERNAN, M. A. & JIMENEZ, J. 1982 Computer analysis of a high-speed film of the plane turbulent mixing layer. *J. Fluid Mech.* **119**, 323–345.

HIGDON, J. J. L. & POZRIKIDIS, C. 1985 The self-induced motion of vortex sheets. *J. Fluid Mech.* **150**, 203–231.

HO, C. M. & HUANG, L. S. 1982 Subharmonics and vortex merging in mixing layers. *J. Fluid Mech.* **119**, 443–473.

HO, C. M. & HUERRE, P. 1984 Perturbed free shear layers. *Ann. Rev. Fluid Mech.* **16**, 365–424.

JACOBS, P. A. 1987 Nonlinear dynamics of piecewise-constant vorticity distributions in an inviscid fluid: Numerical simulations of some prototype flows for the plane mixing layer. Ph.D. thesis, University of Queensland.

JACOBS, P. A. & PULLIN, D. I. 1985 Coalescence of stretching vortices. *Phys. Fluids* **28**, 1619–1625.

JIMENEZ, J. 1983 A spanwise structure in the plane shear layer. *J. Fluid Mech.* **132**, 319–336.

KOOCHESFAHANI, M. M. & DIMOTAKIS, P. E. 1986 Mixing and chemical reactions in a turbulent liquid mixing layer. *J. Fluid Mech.* **170**, 83–112.

KRASNY, R. 1986*a* A study of singularity formation in a vortex sheet by the point-vortex approximation. *J. Fluid Mech.* **167**, 65–93.

KRASNY, R. 1986*b* Desingularization of periodic vortex sheet roll-up. *J. Comput. Phys.* **65**, 292–313.

LIN, S. J. & CORCOS, G. M. 1984 The mixing layer: deterministic models of a turbulent flow. Part 3. The effect of plane strain on the dynamics of streamwise vortices. *J. Fluid Mech.* **141**, 139–178.

LUNDGREN, T. S. 1982 Strained spiral vortex model for turbulent fine structure. *Phys. Fluids* **25**, 2193–2203.

MEIRON, D. I., BAKER, G. R. & ORSZAG, S. A. 1982 Analytic structure of vortex sheet dynamics. Part 1. Kelvin–Helmholtz instability. *J. Fluid Mech.* **114**, 283–293.

MICHALKE, A. 1964 On the inviscid instability of the hyperbolic-tangent velocity profile. *J. Fluid Mech.* **19**, 543–556.

MOORE, D. W. 1978 The equation of motion of a vortex layer of small thickness. *Stud. Appl. Math.* **58**, 119–140.

MOORE, D. W. 1979 The spontaneous appearance of a singularity in the shape of an evolving vortex sheet. *Proc. R. Soc. Lond.* A **365**, 105–119.

MOORE, D. W. & SAFFMAN, P. G . 1975 The density of organized vortices in a turbulent mixing layer. *J. Fluid Mech.* **69**, 465–473.

OSTER, D. 1980. The effect of an active disturbance on the development of the two-dimensional turbulent mixing layer. Ph.D. thesis, Tel-Aviv University.

OSTER, D. & WYGNANSKI, I. 1982 The forced mixing layer between parallel streams. *J. Fluid Mech.* **123**, 91–130.

PATNAIK, P. C., SHERMAN, F. S. & CORCOS, G. M. 1976. A numerical simulation of Kelvin–Helmholtz waves of finite amplitude. *J. Fluid Mech.* **73**, 215–240.

PIERREHUMBERT, R. T. & WIDNALL, S. E. 1982 The two- and three-dimensional instabilities of a spatially periodic shear layer. *J Fluid Mech.* **114**, 59–82.

POZRIKIDIS, C. & HIGDON, J. J. L. 1985 Nonlinear Kelvin–Helmholtz instability of a finite vortex layer. *J. Fluid Mech.* **157**, 225–263.

PULLIN, D. I. & JACOBS, P. A. 1986 Inviscid evolution of stretched vortex arrays. *J. Fluid Mech.* **171**, 377–406.

RAYLEIGH, LORD 1880 On the stability, or instability, of certain fluid motions. *Proc. Lond. Math. Soc.* **11**, 57–70.

RILEY, J. J. & METCALFE, R. W. 1980 Direct numerical simulation of a perturbed, turbulent mixing layer. *AIAA paper* 80-0274.

ROBERTS, F. A., DIMOTAKIS, P. E. & ROSHKO, A. 1982 Kelvin–Helmholtz instability of superposed streams. In *An Album of Fluid Motion*, (ed. M. Van Dyke), figure 146, p. 85. Stanford, California, Parabolic.

ROSHKO, A. 1980 The plane mixing layer: Flow visualization results and three-dimensional effects. In *The Role of Coherent Structures in Modelling of Turbulence and Mixing*, (ed. J. Jimenez). Lecture Notes in Physics, vol. 136, pp. 208–217. Springer.

SAFFMAN, P. G. & BAKER, G. R. 1979 Vortex interactions. *Ann. Rev. Fluid Mech.* **11**, 95–122.

THORPE, S. A. 1971 Experiments on the instability of stratified shear flows: miscible fluids. *J. Fluid Mech.* **46**, 299–319.

WINANT, C. D. & BROWAND, F. K. 1974 Vortex pairing: the mechanism of turbulent mixing-layer growth at moderate Reynolds number. *J. Fluid Mech.* **63**, 237–255.

ZABUSKY, N. J. & DEEM, G. S. 1971 Dynamical evolution of two-dimensional unstable shear flows. *J. Fluid Mech.* **47**, 353–379.

ZABUSKY, N. J., HUGHES, M. H. & ROBERTS, K. V. 1979 Countour dynamics for the Euler equations in two dimensions. *J. Comput. Phys.* **30**, 96–106.